RESEARCH ARTICLE

Key Points:
- We showcase calibrated relocation technique in the Simav-Gediz region of western Turkey
- Systematic discrepancy between centroid and focal depths implies slip initiates in areas of low slip
- No evidence for low-angle normal faulting in regional mechanisms or epicenters

Supporting Information:
- Supporting Information S1

Correspondence to:
E. Karasözen,
ekarasoz@mines.edu

Normal faulting in the Simav graben of western Turkey reassessed with calibrated earthquake relocations

Ezgi Karasözen[1], Edwin Nissen[1], Eric A. Bergman[2], Kendra L. Johnson[1], and Richard J. Walters[3]

[1]Department of Geophysics, Colorado School of Mines, Golden, Colorado, USA, [2]Global Seismological Services, Golden, Colorado, USA, [3]COMET, Department of Earth Sciences, Durham University, Durham, United Kingdom

Abstract Western Turkey has a long history of large earthquakes, but the responsible faults are poorly characterized. Here we reassess the past half century of instrumental earthquakes in the Simav-Gediz region, starting with the 19 May 2011 Simav earthquake (M_w 5.9), which we image using interferometric synthetic aperture radar and regional and teleseismic waveforms. This event ruptured a steep, planar normal fault centered at 7–9 km depth but failed to break the surface. However, relocated main shock and aftershock hypocenters occurred beneath the main slip plane at 10–22 km depth, implying rupture initiation in areas of low coseismic slip. These calibrated modern earthquakes provide the impetus to relocate and reassess older instrumental events in the region. Aftershocks of the 1970 Gediz earthquake (M_w 7.1) form a narrow band, inconsistent with source models that invoke low-angle detachment faulting, and may include events triggered dynamically by the unilateral main shock rupture. Epicenters of the 1969 Demirci earthquakes (M_w 5.9, 6.0) are more consistent with slip on the south dipping Akdağ fault than the larger, north dipping Simav fault. A counterintuitive aspect of recent seismicity across our study area is that the largest event (M_w 7.1) occurred in an area of slower extension and indistinct surface faulting, yet ruptured the surface, while recent earthquakes in the well-defined and more rapidly extending Simav graben are smaller (M_w <6.0) and failed to produce surface breaks. Though our study area bounds a major metamorphic core complex, there is no evidence for involvement of low-angle normal faulting in any of the recent large earthquakes.

1. Introduction

Western Turkey is a rapidly extending continental region with a long history of destructive normal faulting earthquakes including several large instrumentally recorded events. It is bound by the right-lateral North Anatolian fault to the North, the Anatolian plateau to the East, the Cyprus Arc and Hellenic Trench to the South, and the Aegean Sea to the West (Figure 1a). GPS velocities show maximum N-S extension rates of ~30 mm/yr along the Aegean coastline at a longitude of ~27° E, diminishing to zero east of ~32° E [*Aktuğ et al.*, 2009] (Figure 1b). Extension is expressed in the regional topography by a series of approximately E-W trending graben and half graben [e.g., *Sengör*, 1987; *Seyitoğlu*, 1997; *Yılmaz et al.*, 2000], and in crustal thicknesses, which are thinner in western Turkey (25–35 km) than in central and eastern Anatolia (35–45 km and 45–55 km, respectively) [e.g., *Saunders et al.*, 1998; *Karabulut et al.*, 2013; *Tezel et al.*, 2013; *Vanacore et al.*, 2013; *Delph et al.*, 2015; *Kind et al.*, 2015]. In general, normal faults closer to the Aegean have greater relief and longer segment lengths and are presumably at a more advanced stage of development than those bordering the Anatolian plateau in the east (Figure 1a). This gradient in deformation could potentially yield novel insights on the evolution of normal faulting through time. However, a simple space-for-time substitution is complicated by the potential involvement of structures inherited from earlier phases of shortening and extension during the Cenozoic.

The Early Cenozoic history of western Turkey is dominated by northward subduction of Neotethys oceanic lithosphere, concluding in the late Eocene to early Oligocene continental collision of the Anatolide microplate with the southern Eurasian margin [e.g., *Sengör and Yılmaz*, 1981; *van Hinsbergen*, 2010]. Subsequent late Cenozoic extension manifests itself in two distinct styles of deformation: (1) exhumation of the Menderes Massif metamorphic core complex along three major low-angle detachment faults, starting in the latest Oligocene; and (2) ~E-W trending graben formation along high-angle normal faults, starting in the early
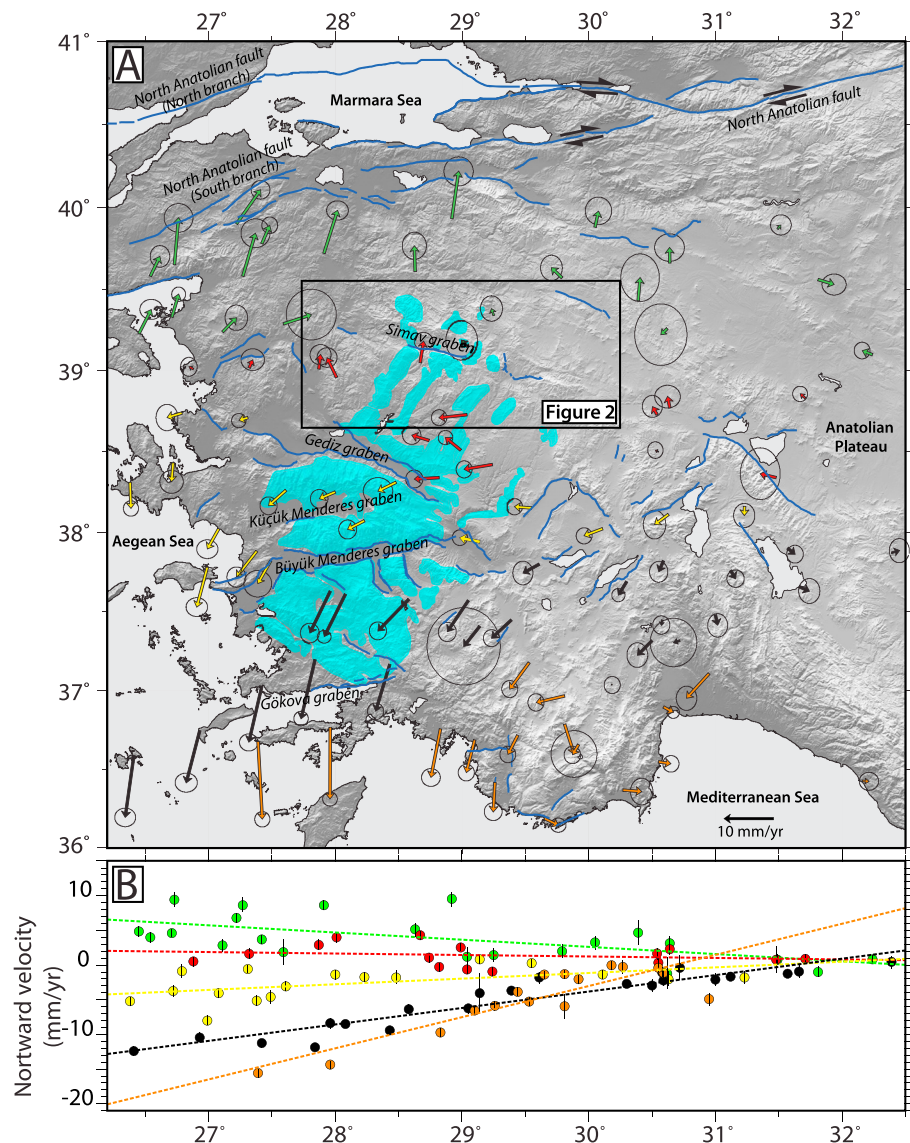
Figure 1. (a) Topography, active faults, and GPS velocities of western Turkey. GPS velocities from *Aktuğ et al.* [2009] are plotted relative to central Anatolia with 95% confidence ellipses and are colored according to position relative to major faults and graben. The study area is outlined by the box, while the cyan-shaded area shows the extents of the Menderes Massif [*van Hinsbergen et al.*, 2010]. Major faults, compiled and modified from *Şaroğlu et al.* [1992] and *Armijo et al.* [2005], are denoted by blue lines. (b) Profile of the northward GPS velocity component, color coded as in Figure 1a. Dashed lines are linear trends through each colored subset of velocities.

Miocene and continuing to the present day [e.g., *Hetzel et al.*, 1995; *Bozkurt and Sözbilir*, 2004; *Thomson and Ring*, 2006; *Hetzel et al.*, 2013]. Possible driving forces of this extension include rollback of northward subducting Mediterranean oceanic lithosphere, gravitational collapse of overthickened continental crust, or changes in regional plate configuration such as opening of the Red Sea [e.g., *McKenzie*, 1978; *Le Pichon and Angelier*, 1979; *Dewey*, 1988; *Seyitoğlu and Scott*, 1991; *Koçyiğit et al.*, 1999; *Bozkurt and Sözbilir*, 2004]. In spite of the dense set of measured GPS velocities, there are conflicting views on whether western Turkey now comprises a small number of rigid microplates [*Nyst and Thatcher*, 2004; *Reilinger et al.*, 2006; *Tiryakioğlu et al.*, 2013] or whether deformation is more evenly distributed across an array of active faults [*Aktuğ et al.*, 2009]. This debate is hindered by incomplete knowledge of the faults responsible for several historical and early instrumental earthquakes and the degree to which structures inherited from earlier phases of deformation influence contemporary kinematics.
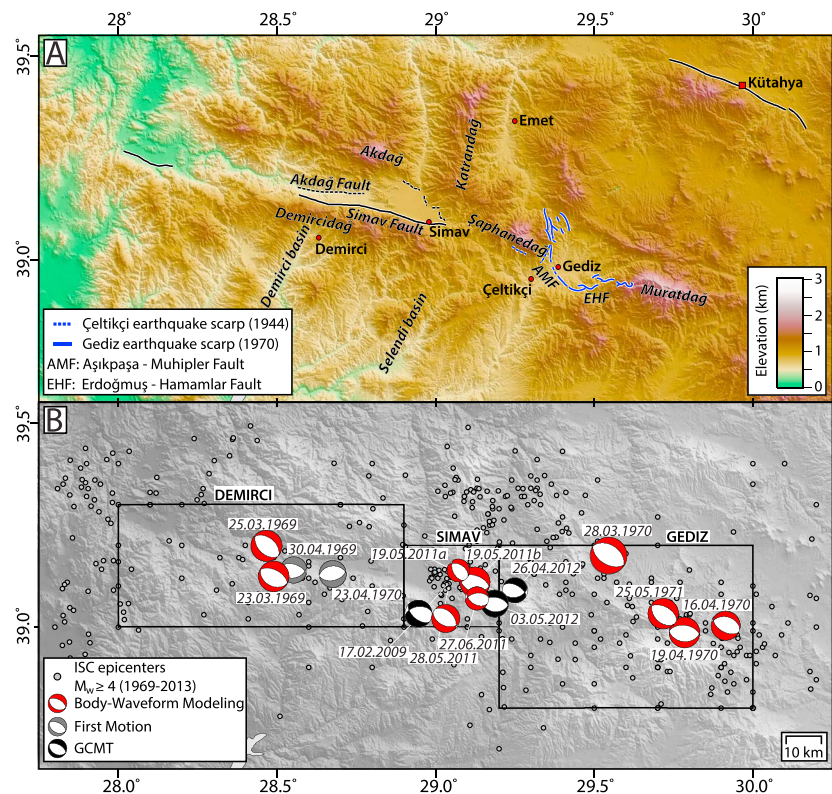
Figure 2. (a) Shaded-relief topography of the study area showing larger towns, physiographic features, faults, and surface ruptures of the 1944 Çeltikçi and 1970 Gediz earthquakes [*Ambraseys and Tchalenko*, 1972]. (b) Earthquakes of $M_w \geq 4.0$ with focal mechanisms where available. Red mechanisms are from teleseismic body waveform modeling, grey mechanisms are from first motions, and black mechanisms are from the Global CMT catalogue; details and references for all these solutions are provided in Tables 1, 5, and 6. Black boxes show the locations of the Simav, Gediz and Demirci clusters in Figures 5, 8, and 9, respectively.

In this study, we investigate a series of large earthquakes in the Simav-Gediz region (Figures 1a and 2) which, if properly characterized, could help address these controversies. We start by characterizing the recent M_w 5.9 Simav earthquake of 19 May 2011 and its aftershock sequence using an assortment of modern data which include synthetic aperture radar interferometry (InSAR) and dense regional seismic recordings. This event is then used as a catalyst to reassess older instrumental events in the region using an improved calibrated earthquake relocation method. Of particular interest to us are the M_w 7.1 Gediz earthquake of 28 March 1970, which is among the largest continental normal faulting earthquakes recorded globally and the largest in western Turkey, and the M_w 5.9 and M_w 6.0 Demirci earthquakes of 23 and 25 March 1969, which are the next largest instrumental events in this region. The faults responsible for these older events remain unclear due in part to large epicentral uncertainties, and there have been controversial suggestions that basal, low-angle detachment faults were involved [*Eyidoğan and Jackson*, 1985; *Braunmiller and Nábeělek*, 1996; *Seyitoğlu*, 1997; *Gürboğa*, 2013]. Because the faulting is so poorly characterized, the risks posed to nearby cities are also little understood.

2. Geological and Tectonic Setting

Our study is focused on the area surrounding the towns of Simav and Gediz in southwestern Kütahya province. The dominant physiographic feature in the area is the Simav graben, a ~50 km long, up to ~10 km wide, approximately E-W trending basin bounded by normal faulting on both margins (Figure 2). The north dipping Simav fault on the southern margin is straighter and exhibits greater relief (~1000 m) than faulting along the northern margin. It has a reported average dip of 45°–50°, though surface exposures of the fault plane are rare [*Seyitoğlu*, 1997]. National active fault databases assign the Simav fault a significant right-lateral component [*Şaroğlu et al.*, 1992; *Emre et al.*, 2011]. Its footwall comprises the strongly asymmetric Demircidağ range, characterized by a steep north facing slope adjacent to the Simav graben and a gentle south facing slope.

The latter follows the latest Oligocene to early Miocene Simav detachment fault, which exposes metamorphic rocks of the Menderes Massif and is cut by the N-S trending Demirci and Selendi basins, whose sedimentary and volcanic rocks record a later phase of extension in the middle Miocene [*Seyitoğlu*, 1997; *Yılmaz et al.*, 2000; *Işık and Tekeli*, 2001; *Purvis and Robertson*, 2004; *Thomson and Ring*, 2006]. South dipping faulting on the northern side of the Simav graben, which we hereby refer to as the Akdağ fault but which may actually comprise several discontinuous fault segments, is less well developed than the north dipping Simav fault. Its footwall lacks the steep range front of the Demircidağ, despite being made of harder rocks (early Miocene granites, volcanics, and sediments). Despite the physiographic asymmetry of the Simav graben, there is still some debate over which of its bounding faults is dominant. The graben floor tilts northward and its trunk stream (the Simav River) hugs its northern side, as if controlled by the south dipping Akdağ fault [*Eyidoğan and Jackson*, 1985]. However, *Westaway* [1990] proposed that the north dipping Simav fault dominates on the basis of southward dipping Neogene sediments exposed along the southern side of the basin.

East of the Simav graben, the surface expression of active faulting becomes much less distinct. Lowlands surrounding the town of Gediz comprise Middle Miocene to Early Pliocene interbedded limestones, marls, sandstones and volcanics, and, in contrast with the Simav graben lack a thick Quaternary basin fill [*Gürboğa-Deveci et al.*, 2013]. Surrounding mountain ranges include the Şaphanedağ to the West of Gediz and Muratdağ to the southeast, both of which comprise metamorphic rocks of the Menderes Massif. The E dipping Aşıkpaşa-Muhipler fault zone, which ruptured during the 1970 Gediz earthquake, bounds the eastern slope of the Şaphanedağ yet is poorly defined in the landscape [*Ambraseys and Tchalenko*, 1972]. The northern slope of Muratdağ is defined by a set of north dipping normal faults, of which the Erdoğmuş-Hamamlar fault also ruptured during the 1970 earthquake [*Ambraseys and Tchalenko*, 1972; *Gürboğa*, 2013].

There are written records of two major historical earthquakes in the study area. An earthquake on 18 April 1896 destroyed many houses in the Emet region (Figure 2), but there are no firm estimates of its epicenter or magnitude [*Taşdemiroğlu*, 1971]. The Çeltikçi earthquake on 25 June 1944 caused severe damage to villages on the eastern and southern flanks of Şaphanedağ, where there were also some reports of discontinuous surface rupturing; the magnitude has been estimated as ∼6 [*Taşdemiroğlu*, 1971; *Ambraseys and Tchalenko*, 1972; *Ambraseys and Jackson*, 1998]. Instrumentally recorded events (Figure 2) can be divided into three clustered sequences: (1) the 2011 Simav sequence in the eastern Simav graben, which includes the 19 May 2011 M_w 5.9 earthquake; (2) the Gediz sequence starting with the 28 March 1970 M_w 7.1 earthquake, in the eastern part of our study area; and (3) the Demirci sequence starting with M_w 5.9 and M_w 6.0 events in 1969 in the western Simav depression.

3. The 19 May 2011 Simav Earthquake

The 19 May 2011 Simav earthquake (M_w 5.9) occurred close to the eastern end of the Simav graben (Figure 2). Despite the moderate size, two people were killed, ∼100 people were injured, and ∼2000 households were heavily damaged or collapsed [*Zülfikar et al.*, 2011]. Published focal mechanisms from several sources consistently indicate WNW-ESE normal faulting with nodal plane dips in the range 30°–60° (Table 1). Although minor cracking was observed in two locations west of Simav, approximately coincident with the north dipping Simav fault, there were no clear indications of primary surface rupturing [*Zülfikar et al.*, 2011; *Demirci et al.*, 2015]. Aftershocks relocated with the double-difference technique do not align along a clear rupture plane [*Görgün*, 2014; *Demirci et al.*, 2015], and hence, the dip direction of the causative fault is unclear. Body waveform modeling by *Yolsal-Çevikbilen et al.* [2014] indicates a centroid depth of ∼9 km, also consistent with the lack of surface ruptures. The main shock was preceded by a M_w ∼5.1 event on 17 February 2009 in approximately the same location and a smaller, M_w 4.4 foreshock which occurred 15 min before the main shock (Table 1).

In this section we reanalyze the Simav earthquake using new seismological observations and modeling complemented by the first measurements of its surface deformation from InSAR. Our aims are to better constrain the location and orientation of the causative fault and to investigate the possible involvement of low-angle or listric structures which may not be captured in the simple point source, double-couple models published for this event.

3.1. Teleseismic Body Waveform Modeling
We used long-period teleseismic body waveform modeling to determine the main shock source parameters. Broadband seismograms recorded by the Global Digital Seismic Network were deconvolved to give an

Table 1. Source Parameters of Instrumentally Recorded Events in the Simav Region During the Period 2009–2012 Whose Focal Mechanisms Have Been Determined[a]

Date	Time (UTC)	Latitude	Longitude	Depth (km)	Moment (Nm)	M_w	Strike1 (°)	Dip1 (°)	Rake1 (°)	Strike2 (°)	Dip2 (°)	Rake2 (°)	Reference	Data used
17-02-2009	05:28:22	39.13[h]	29.05[h]	15.5[h]	-	$4.8m_b$	-	-	-	-	-	-	ISC	Global traveltimes
	05:28:19	39.11[h]	29.04[h]	7.3[h]	-	5.2	-	-	-	-	-	-	NEIC	Global traveltimes
	05:28:24	**39.15[c]**	**28.98[c]**	**16.8[c]**	**8.14×10^{16}**	**5.2**	**262**	**46**	**−128**	**131**	**55**	**−57**	**CMT**	**Global long-period surface waves**
	-	-	-	12.0[c]	3.59×10^{16}	4.9	145	55	0	55	90	145	NEIC-M_wr	Regional moment tensor
19-05-2011a	-	39.12[h]	29.10[h]	7.8[h]	-	$3.4m_b$	-	-	-	-	-	-	ISC	Global traveltimes
19-05-2011a	**19:59:47**	**39.13[h]**	**29.10[h]**	**10.0[h]**	**5.82×10^{15}**	**4.4**	**300**	**45**	**−105**	**141**	**47**	**−75**	**G14**	**HypoDD—Regional moment tensor**
19-05-2011b	20:15:25	39.13[h]	29.07[h]	11.7[h]	-	$5.8m_b$	-	-	-	-	-	-	ISC	Global traveltimes
	20:15:22	39.15[h]	29.10[h]	7.0[h]	-	5.8	-	-	-	-	-	-	NEIC	Global traveltimes
	20:15:25	39.08[c]	29.11[c]	12.1[c]	8.75×10^{17}	5.9	286	46	−85	98	44	−96	CMT	Global long-period surface waves
				11.0[c]	6.79×10^{17}	5.8	262	58	−122	131	44	−50	NEIC-M_wr	Regional moment tensor
				15.0[c]	6.69×10^{17}	5.8	275	37	−103	111	54	−81	NEIC-M_ww	Regional and teleseismic, very long period
		39.15[h]	29.08[h]	10.0[h]	1.15×10^{18}	6.0	285	60	−90	105	30	−90	G14	HypoDD—Regional moment tensor
				9.0[c]	6.8×10^{17}	5.9	287	58	−94	115	32	−83	YÇ14	Teleseismic long-period body waves
						-	287	58	−94	115	32	−83	YÇ14	Teleseismic and regional P wave first motions
				10.0[c]	6.83×10^{17}	5.9	278	55	−97	110	36	−80	YÇ14	Teleseismic, long-period P waves
				8.0[c]	**5.08×10^{17}**	**5.8**	**289**	**54**	**−93**	**112**	**37**	**−87**	**K16**	**Teleseismic, long-period body waves**
				7.0[c]	4.68×10^{17}	5.8	285	54	−80	88	36	−104	K16	Regional moment tensor
28-05-2011	05:47:18	39.13[h]	28.99[h]	13.3[h]	-	$4.9m_b$	-	-	-	-	-	-	ISC	Global traveltimes
	05:47:17	39.12[h]	29.05[h]	9.2[h]	-	4.8	-	-	-	-	-	-	NEIC	Global traveltimes
	05:47:19	39.09[h]	29.04[h]	14.1[h]	4.78×10^{16}	5.1	314	45	−65	100	51	−113	CMT	Global long-period surface waves
	-	-	-	9.0[c]	2.24×10^{16}	4.8	296	51	−87	111	39	−96	NEIC-M_wr	Regional moment tensor
	-	**39.11[h]**	**29.06[h]**	**17.0[h]**	**1.25×10^{17}**	**5.4**	**315**	**45**	**−75**	**114**	**47**	**−105**	**G14**	**HypoDD—Regional moment tensor**
27-06-2011	21:14:00	39.14[h]	29.04[h]	12.7[h]	-	$4.7m_b$	-	-	-	-	-	-	ISC	Global traveltimes
	21:13:58	39.1[h]	29.03[h]	10.4[h]	-	4.7	-	-	-	-	-	-	NEIC	Global traveltimes
	21:14:01	39.07[c]	29.13[c]	19.3[c]	4.09×10^{16}	5.0	313	55	−66	95	42	−120	CMT	Global long-period surface waves
	-	-	-	10.0[c]	1.57×10^{16}	4.7	315	60	−60	86	41	−131	NEIC-M_wr	Regional moment tensor
	-	**39.12[h]**	**29.02[h]**	**20.0[h]**	**5.62×10^{15}**	**4.5**	**261**	**57**	**−117**	**124**	**41**	**−55**	**G14**	**HypoDD—Regional moment tensor**
26-04-2012	22:05:35	39.16[h]	29.11[h]	8.3[h]	-	$4.6m_b$	-	-	-	-	-	-	ISC	Global traveltimes
	22:05:33	39.12[h]	29.08[h]	8.0[h]	-	4.6	-	-	-	-	-	-	NEIC	Global traveltimes
	22:05:35	**39.09[h]**	**29.25[h]**	**13.6[h]**	**2.14×10^{16}**	**4.8**	**296**	**55**	**−66**	**79**	**42**	**−120**	**CMT**	**Global long-period surface waves**
				7.0[c]	1.16×10^{16}	4.7	300	70	−65	66	31	−139	K16	Regional moment tensor
03-05-2012	15:20:25	39.18[h]	29.09[h]	3.1[h]	-	5.2	-	-	-	-	-	-	NEIC	Global traveltimes
	15:20:27	**39.06[c]**	**29.17[c]**	**12.0[c]**	**8.89×10^{16}**	**5.2**	**277**	**51**	**−91**	**98**	**39**	**−88**	**CMT**	**Global long-period surface waves**
	-	-	-	8.0[c]	7.32×10^{16}	5.2	284	65	−89	101	25	−93	NEIC-M_wb	Body wave moment tensor

[a] h and c are hypocenter and centroid parameters, respectively. References are G14—Görgün [2014], YÇ14—Yolsal-Çevikbilen et al. [2014], and K16—this study. Focal mechanisms displayed in Figure 2b are shown inbold.

equivalent response of World-Wide Standardized Seismograph Network 15–100 s long-period instruments, in order to remove high-frequency noise and so that the source can be represented as a point in space (the centroid). In order to avoid complications from Earth's crust and outer core, we only used waveforms in the distance range 30°–90°. Then, we used the MT5 version [*Zwick et al.*, 1994] of the weighted least squares algorithm of *McCaffrey and Abers* [1988] and *McCaffrey et al.* [1991] to invert the *P* and *SH* waveforms to find the best fit strike, dip, rake, scalar moment, centroid depth, and source time function. Synthetic waveform amplitudes were corrected for geometrical spreading [*Langston and Helmberger*, 1975] and for anelastic attenuation, with a t^* (the ratio of traveltime to average *Q*) of 1.0 s for *P* and 4.0 s for *SH* waves [*Futterman*, 1962]. Uncertainties in t^* affect source duration and moment but have negligible influence on other source parameters [*Fredrich et al.*, 1988; *Maggi et al.*, 2000]. We modeled *P*, *pP*, and *sP* phases on 25 s vertical component seismograms and *S* and *sS* phases on 30 s transverse component seismograms, weighted the seismograms according to azimuthal density, and halved the weighting of the *SH* waveforms to account for their larger amplitudes. We assumed an elastic half-space with $V_p = 5.3$ km s^{-1}, $V_s = 3.3$ km s^{-1}, and density 2600 kg m^{-3}, values chosen on the basis of the local velocity structure obtained from our calibrated relocation analysis in section 4. Arrival times were checked against broadband records before the inversion, to prevent any potential biases that could arise from traveltime anomalies.

Though our modeling approach is very similar to that of *Yolsal-Çevikbilen et al.* [2014], their modeled *P* seismograms contain a large (168°) azimuthal gap and they only incorporate three *SH* records. We use a more even *P* seismogram spacing including several at southern azimuths and also include 22 *SH* seismograms, which provide additional sensitivity to changes in fault orientation. Our model also uses seismogenic layer velocities that are determined by available near-source data.

Our solution for the Simav earthquake has a clear ∼WNW-ESE trending normal mechanism (parallel to the local strike of the Simav fault) and is similar to other published solutions, with discrepancies in strike, dip, and rake of no more than 30°, 20° and 30°, respectively (Figure 3 and Table 1). The NNE dipping nodal plane is slightly steeper (54°) than the SSW dipping plane (37°) and neither exhibits a significant strike-slip component, in contrast with published fault maps of the area [*Şaroğlu et al.*, 1992; *Emre et al.*, 2011]. Our centroid depth of 8 km is shallower than the *Yolsal-Çevikbilen et al.* [2014]'s solution of 9 km but consistent given their choices of seismic velocity ($V_p = 6.8$ km/s, $V_s = 3.9$ km/s). To investigate uncertainties in key parameters, we run further inversions in which individual parameters are fixed incrementally on either side of their minimum misfit values, and the resulting model errors are compared to the best solution [e.g., *Molnar and Lyon-Caen*, 1989; *Taymaz et al.*, 1991]. We find that the strike can be altered by $\pm 15°$ and the centroid depth by ± 2 km before any clear, visual degradation to the seismogram misfits can be detected (Figure S1 in the supporting information).

We also investigated whether the Simav earthquake involved listric faulting, as has been proposed for some other earthquakes within Western Turkey [e.g., *Taymaz and Price*, 1992]. We followed a similar modeling procedure to those used by *Eyidoğan and Jackson* [1985] and *Braunmiller and Nábeělek* [1996] in their studies of earlier events in this region. To simulate rupture of a listric (upward concave) fault, we represented the earthquake as three separate point sources with dips and depths fixed at 35° and 11 km, 55° and 9 km, and 75° and 7 km and with strikes and rakes fixed to the values of the single point source solution. The moments, source time functions, and relative timing of the three source events were then allowed to vary in a series of inversions. No matter which subevent was allowed to rupture first, normalized errors were larger than for the single event solution. Furthermore, almost all of the moment release was forced onto the middle (55° dipping) fault plane. Lastly, our preferred teleseismic (single-event) waveform model is consistent with first motions recorded on regional seismograms [*Yolsal-Çevikbilen et al.*, 2014], which represent the initial seismic energy radiation, presumably at or near the base of the fault (Table 1). In summary, all available evidence supports slip on a planar, moderately dipping fault, and there is no indication of significant slip on a lower angle or listric structure.

3.2. Regional Waveform Modeling

For an independent check on the Simav main shock focal mechanism and centroid depth, we performed a regional moment tensor (RMT) analysis using *Herrmann et al.* [2011]'s methodology. This technique uses surface wave spectral amplitudes and radiation patterns recorded at regional distances and is therefore independent from the teleseismic body waveform modeling employed in the previous section. By matching the larger amplitude surface waveforms, in addition to the *P* and *S* body waves, earthquakes as small as M_w ∼4
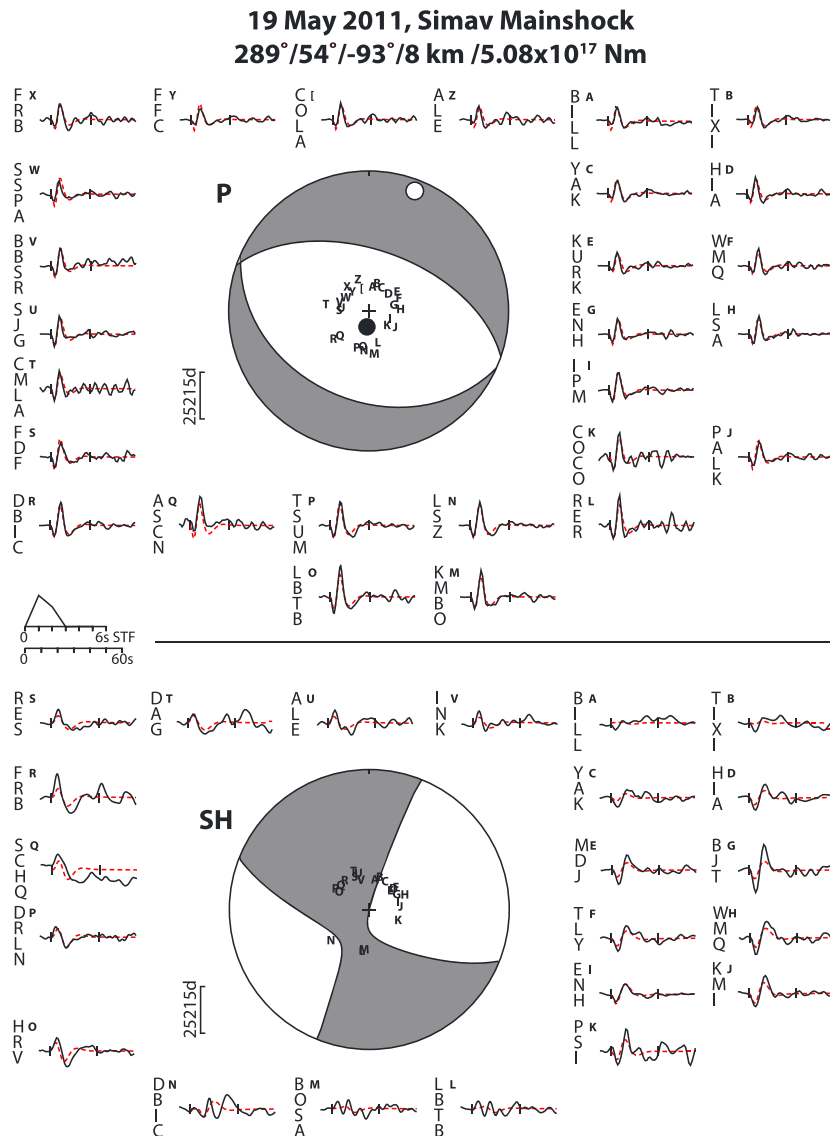
Figure 3. Minimum misfit solution for the 19 May 2011 Simav earthquake calculated by inverting long-period *P* (upper panel) and *SH* (lower panel) teleseismic body waves. Numbers below the event date show the strike, dip, and rake of the NNE dipping nodal plane; the centroid depth in kilometers; and the moment in Nm. Observed (black solid) and synthetic (red dashed) waveforms are plotted around the focal spheres with the inversion window indicated by vertical ticks. These stations are ordered clockwise by azimuth, with station codes written vertically. Stations are denoted by capital letters on the focal spheres. The source time function (STF) is plotted between two focal spheres, with the waveform time scale below it. The amplitude scales for the waveforms are shown with vertical bars next to each focal sphere in microns and the lowercase letter "d" indicates the instrument type (Global Digital Seismographic Network (GDSN) long period). *P* and *T* axes are represented by solid and open circles, respectively, on the *P* wave radiation pattern.

can be examined in this way. The RMT inversion scheme assumes a step function for the moment release and treats each event as a point source, which is reasonable for earthquakes of this magnitude or smaller. The first stage of the modeling uses an assumed velocity model to compute Green's functions from the source to each receiver. Next, at 1 km increments in centroid depth, the observed waveform trace is compared with synthetic waveforms computed for each receiver. To obtain best fitting parameters, a grid search is performed over all values of strike, dip, and rake angles at 10° increments, followed by a 5° search in a region ±20 about the best fit [*Herrmann et al.*, 2011].

We used high quality broadband waveform data recorded by 34 stations of the National Seismic Network of Turkey over the distance range 100–600 km, which provided excellent azimuthal coverage (Figure S2).

Table 2. The Crustal Model Determined by and Used in the Earthquake Relocation, as Described in Section 4 (Figure S4)[a]

Depth to Top of Layer (km)	P Velocity (km s^{-1})	S Velocity (km s^{-1})
0	5.30	3.30
12	5.60	3.45
16	5.90	3.50
35	7.90	4.50

[a]The ak135 velocity model is used for all noncrustal phases at all epicentral distances [*Kennett et al.*, 1995].

These were filtered using a 0.025–0.06 Hz passband. Green's functions were computed using the local velocity model obtained from our calibrated relocation analysis in section 4 (Table 2). Our best fit focal mechanism (Figure S2) is in excellent agreement with the one obtained from teleseismic body waveform analysis, with discrepancies of 4° in strike, 1° in dip, 13° in rake, and 1 km in centroid depth (Table 1).

3.3. InSAR

Ground deformation measured with InSAR provides a third set of independent constraints on the earthquake source mechanism and allows us to determine more precisely the location and depth extent of the ruptured fault plane. A coseismic interferogram of the Simav earthquake was constructed from using the Jet Propulsion Laboratory (JPL)/Caltech Repeat Orbit Interferometry PACkage (ROI-PAC) software ENVISAT descending track scenes acquired on 6 May 2011 and 15 June 2011, with a center scene incidence angle of 41° measured from the vertical (Figure 4a). The perpendicular baseline of 400 m is much larger than ideal and may be the source of noise in coherent parts of the interferogram and decorrelation over mountainous areas. Nevertheless, the interferogram displays a clear, elliptical, WSW-ENE trending pattern of fringes, containing peak displacements of three radar half wavelengths (~8.5 cm) away from the satellite. There is no sharp phase discontinuity along either margin of the fringe ellipse, implying that faulting failed to break the surface [e.g., *Lohman et al.*, 2002], in agreement with the lack of field observations of primary surface rupturing. Thus, the surface projection of the faulting might be either at the northern or at the southern edge of the elliptical fringe pattern. Furthermore, the interferogram contains considerable noise, with amplitudes exceeding one fringe in places, and displacement of the footwall block is thus impossible to observe. As the fringe spacing on each long edge of the ellipse is roughly the same, the dip direction of the responsible fault is also unclear [e.g., *Lohman et al.*, 2002].

We generated a series of elastic dislocation models [*Okada*, 1985] and synthetic interferograms by inverting the interferometric data to find the best fitting source parameters [*Wright et al.*, 1999]. We assumed slip on a single, rectangular fault buried in an elastic half space with Lamé parameters $\mu = \lambda = 3.2 \times 10^{10}$ Pa and a Poisson ratio of $\nu = 0.25$, and we tested, separately, both north and south dipping planes. As is common for earthquakes on blind faults, we found a strong trade-off between fault slip and down-dip fault width, and for the models presented here we have assumed a fixed slip magnitude of 0.5 m. The top and bottom depths of the uniform slip model faults should therefore be considered approximate only although its center depth is robust to plausible changes in slip magnitude. Due to the moderate earthquake magnitude, the significant atmospheric noise, and the single available look direction, we do not attempt a variable slip model nor do we further test listric fault geometries, given that the imaging geometry of SAR satellites is insensitive to northward or southward motions.

The strikes of our minimum misfit InSAR model faults did not agree closely with the nodal plane strikes of our teleseismic or regional waveform solutions. Upon further testing, we found that body waveform models are most sensitive to changes in fault orientation, and so in our final InSAR models we fixed the strike to match those of the body waveform nodal planes (289° and 117°, labeled Models A and B in Figures 4c and 4e, respectively and in Table 3). Residual (observed minus model) displacements for both north and south dipping faults are less than one fringe (Figures 4d and 4f). InSAR model faults have somewhat shallower dips (36–38°) than the waveform-based solutions and also include a small component of left-lateral slip (Table 3). The top and bottom depths of the model fault planes are ~6 km and ~10.5 km, respectively, and the center depth of 8–9 km is therefore in good agreement with the centroid depths obtained from modeling both teleseismic and regional waveforms. The north dipping fault (Model A) is in a location consistent with clear
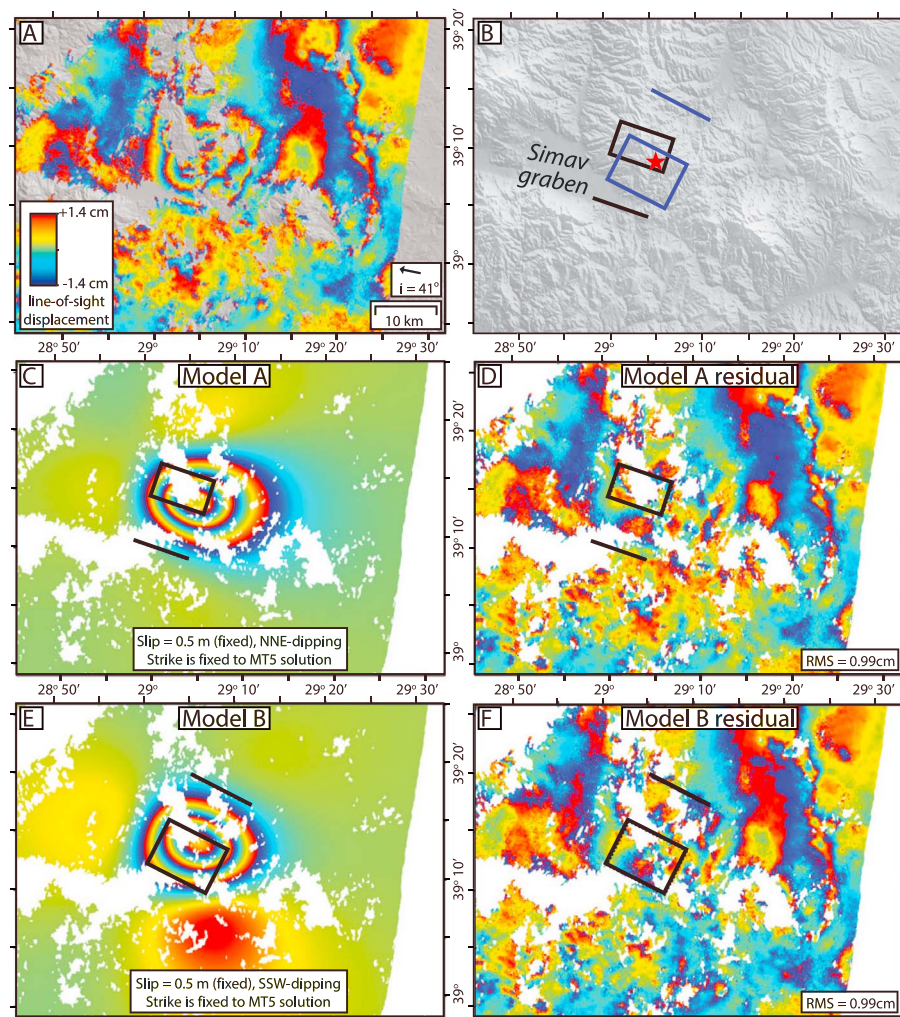
Figure 4. (a) Coseismic interferogram constructed from ENVISAT descending track scenes from 16 May 2011 to 15 June 2011 using the JPL/Caltech ROI-PAC software [*Rosen et al.*, 2004]. *i* is the line-of-sight (LOS) vector, with a center scene incidence angle of 41° measured from the vertical. Positively increasing values within each color cycle indicate increasing LOS displacement toward the satellite. (b) Conjugate model faults overlain on shaded topography. The boxes show the rectangular model faults in plan view and the lines show their up-dip surface projections. (c) Model and (d) residual (observed minus model) interferogram for a NNE dipping model fault. (e) Model and (f) residual (observed minus model) interferogram for a SSW dipping model fault.

faulting expressed in the topography, aligning closely with the eastern end of the north dipping Simav fault (Figure 4b), whereas the south dipping fault projects to the surface among mountainous topography with no indication of surface faulting. This strongly implies that it was the north dipping Simav fault that ruptured during the 19 May 2011 earthquake.

Table 3. InSAR Model Fault Parameters for the 19 May 2011 Simav Main Shock[a]

Model	Strike	Dip	Rake	Slip (m)	Latitude	Longitude	Length (km)	Top (km)	Bottom (km)	Center (km)	Moment (Nm)	M_w	RMS (cm)
A	289[b]	38	290	0.5[a]	39.075	29.023	8.9	5.8	10.0	7.9	1.00×10^{18}	5.9	0.99
B	117[a]	36	298	0.5[a]	39.218	29.138	10.3	5.8	11.4	8.6	1.60×10^{18}	6.1	0.99

[a]Latitude and Longitude represent the surface projection of the center of the model fault plane. Top, Bottom, and Center are the depths of the top, bottom, and center of the uniform slip (0.5 m) model fault plane, respectively. RMS is the root-mean-square misfit between model and observed displacements.
[b]Fixed in inversion.

4. Regional Seismicity From Calibrated Earthquake Relocations

In this section we reassess earthquake hypocenter locations across the wider Simav-Gediz region by analyzing clusters of earthquakes with the mloc multiple-event relocation technique [*Bergman and Solomon*, 1990; *Walker et al.*, 2011], which is a based on the hypocentroidal decomposition (HD) method of *Jordan and Sverdrup* [1981]. Like many other methods of multiple-event location, mloc estimates improved relative locations of clustered events by minimizing path-correlated errors in theoretical traveltimes. Unlike other methods, mloc has been specialized to determine calibrated locations when appropriate data sets are available. A calibrated event is one for which the location bias (in an absolute sense) from unknown Earth structure has been minimized and for which location uncertainty has been quantified. The problem of unknown Earth velocity structure is reduced in multiple-event relocation methods by assuming that ray paths from a close spatial cluster of events largely sample the same portion of Earth, such that the differences in traveltimes mostly reflect the relative hypocenter locations. It is important to distinguish the improvement in relative locations provided by all methods of multiple-event relocation from the question of the accuracy of the relocated cluster as a whole in absolute terms. Our concept of calibration addresses that question. Whether or not these relative locations can then be calibrated usually depends on the availability of near-source data, and western Turkey is excellent in this regard as it has had dense station coverage since the early 2000s (e.g., Figure S3). This allows us to use a subset of well-recorded modern events to calibrate clusters that include older earthquakes.

The HD algorithm divides the relocation procedure into two independent inverse problems, and one advantage of mloc over other relocation procedures is that each step may exploit an independent data set. (1) It solves for the "cluster vectors" that describe the relative location of each individual event with respect to the geometric center of the cluster, which is called the "hypocentroid." This step can utilize all available data at any epicentral distance. (2) Then, it solves for the location of the hypocentroid, which establishes the absolute coordinates of all events in the cluster. This could be done using the same set of readings that were used to esti-mate the cluster vectors, but such a solution would not be considered "calibrated" because of the significant uncertainties in theoretical traveltimes over large distances. For our calibrated locations we used direct arrival phases (*Pg* and *Sg*) at short epicentral distances only (<2°), with readings normally selected up to the nearest distance for which a good azimuthal coverage is achieved. By keeping ray path lengths short, the accumulated traveltime error from unknown velocity structure and the possible location error are minimized. Cluster vectors are more bias-free than the hypocentroid location since they are determined from traveltime differences. The two steps are repeated and usually converge upon a stable solution after two to four iterations.

An additional advantage of mloc over other relocation methods is its rigorous characterization of errors from a variety of sources. After gross outlier readings are removed, empirical reading errors are estimated from the actual data set using multiple samples of each station-phase pair, using a robust estimate of spread [*Croux and Rousseeuw*, 1992; *Ghods et al.*, 2012]. The scatter in residuals carries information about traditional picking uncertainties and other sources of error and is used to weight the data and to identify additional outliers [*Ghods et al.*, 2012; *Aziz Zanjani et al.*, 2013]. In this way, the data set is cleaned iteratively until the spread of residuals resembles an approximate Gaussian distribution. In the inversion, residual traveltimes are weighted inversely to the empirical reading error determined for that station phase.

In the earthquake relocation problem, the greatest uncertainty is usually encountered for focal depth and origin time (because it is strongly coupled to focal depth) since their resolution depends on the accuracy of the velocity model and the availability of suitable depth-sensitive phases. Focal depths can be estimated with higher resolution by using teleseismic depth phases (*pP*, *sP*, *sS*) or by using near-source direct phase arrivals (*Pg*, *Sg*). Depth phases are most useful for deeper teleseismic events, but shallower event depths are harder to resolve due to the difficulties in phase identification, which can make the probability den-sity function bi-modal [*Bergman*, 2014]. For local events, *Pg* and *Sg* phases up to distances of several times the focal depth provide strong depth constraint and in that case the HD method can treat depth as a free parameter with uncertainties of <3 km [*Aziz Zanjani et al.*, 2013; *Bergman*, 2014]. In many cases, however, free-depth solutions are unstable for at least some events in a cluster and it is preferable to set depths manually (minimizing residuals at nearby stations) and perform fixed depth relocations. From the well-constrained events we calculate a default depth which is applied to events that have no readings at nearby stations.
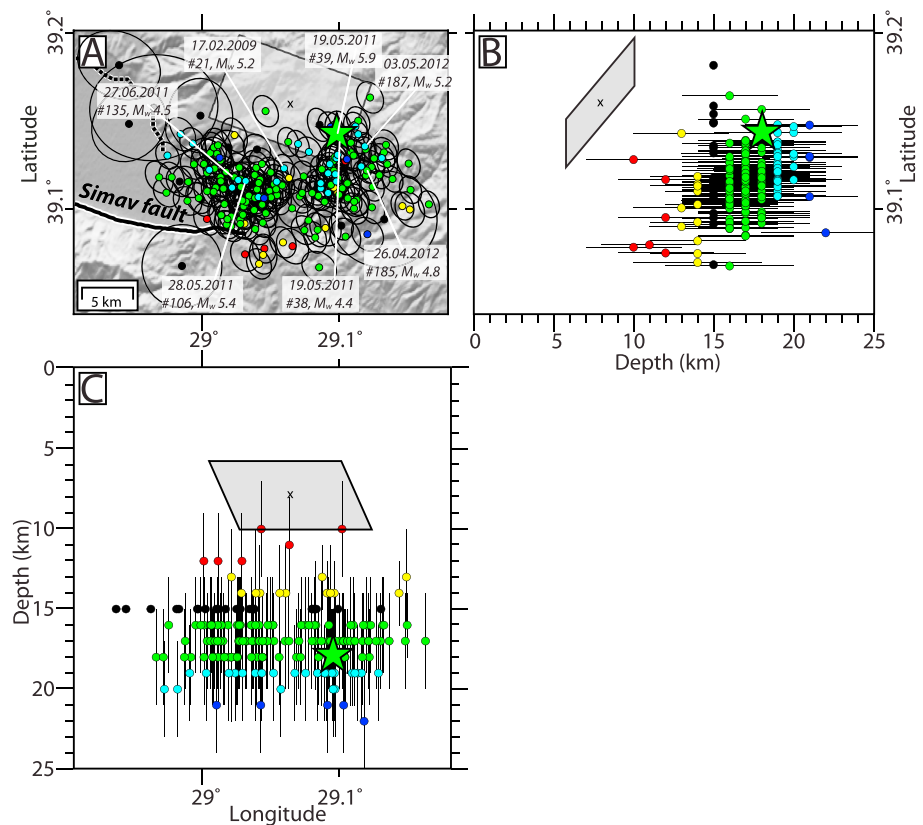
Figure 5. (a) Earthquake hypocenters in the Simav cluster, colored according to their depth (black circles are older events of uncertain depth). Numbers denote earthquakes with focal mechanisms in Tables 1 and S1. Each hypocenter is shown with its 90% confidence ellipse. The gray rectangle indicates the location of InSAR fault Model A (Figure 4), and the green star denotes the 19 May 2011 Simav main shock hypocenter. (b) N-S and (c) E-W vertical profiles through the same data, with hypocenters colored by depth as in Figure 5a and lines indicating their depth uncertainties. The gray parallelograms show the projections of InSAR fault Model A onto the profiles.

This is often the case for older events. Errors in focal depth do not affect epicenter locations unless greater than ∼15 km [*Ghods et al.*, 2012].

Older earthquakes (1960s–1990s) can be relocated together with modern events if they share readings from the same stations. In order to provide this connectivity within our study area, which contains many important 1960s and 1970s earthquakes as well as well-recorded modern ones, we started by relocating recent events with a fixed cluster depth that minimizes the trade-off between the available arrival times and the predicted traveltimes. This depth is kept fixed until the cluster is stable and outliers are removed. Then, the focal depth of each event with near-source readings is set by manually fitting the residuals or a free-depth solution is performed if the cluster is well connected. When the older events are introduced into the stable cluster decade by decade, their depths are kept fixed.

In our study, all relocations are based on the same 1-D Earth model (Table 2) which is a composite of a custom crustal model over the 1-D global average model ak135 [*Kennett et al.*, 1995]. For a single event recorded at a handful of stations, location trades off strongly with velocity, but by using hundreds of readings from multiple events with fixed relative locations, a stable velocity structure can be obtained. For crustal phases (*Pg*, *Sg*), *P* wave and *S* wave velocities are adjusted to fit the available arrival data in the source region. Because the azimuthal coverage at short distances for the cluster as a whole is very good, the hypocentroid is stable with respect to changes in the local velocity structure. We find that the best fit is obtained with a three-layered crust with *P* and *S* wave velocities of 5.3 km s^{-1} and 3.3 km s^{-1} for the top 12 km and 5.6 km s^{-1} and 3.45 km s^{-1} for 12–16 km depth. Lower crustal velocities (5.9 km s^{-1} and 3.5 km s^{-1}) and crustal thickness (35 km) are determined by fitting observed *Pn* and *Sn* arrival times after crustal velocities and focal depths have already been determined (Figure S4). Our estimated crustal thicknesses of 38 km (Simav) and 35 km (Gediz and Demirci) are
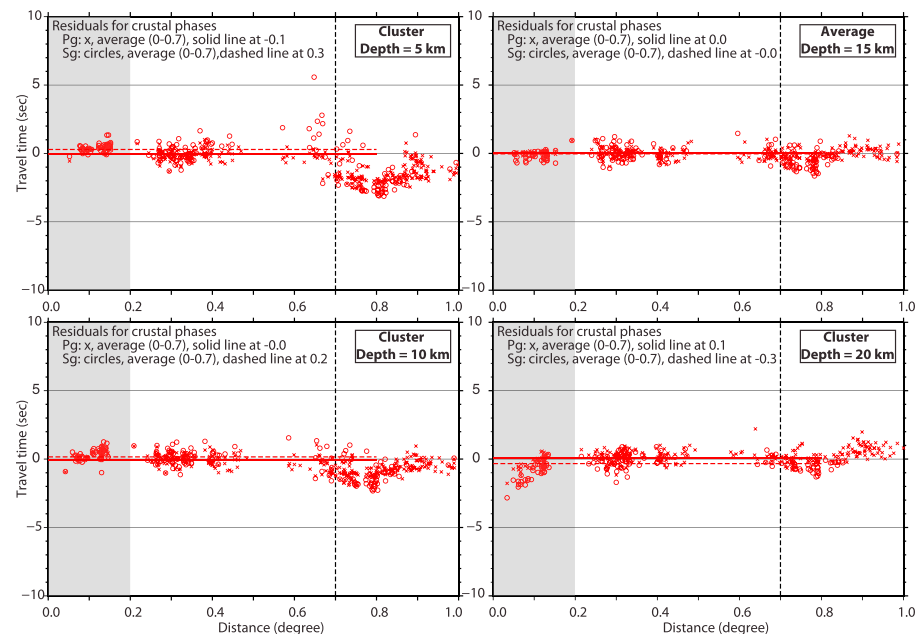
Figure 6. The fit between observed phase arrivals and theoretical traveltimes calculated from the local velocity model (Table 2) at near-source distances for different cluster depths. The shaded area shows the distance range that is most sensitive to focal depth. *Pg* arrivals are indicated by red crosses and *Sg* by open red circles. Solid and dashed horizontal lines indicate average residuals for *Pg* and *Sg*. The vertical dashed line shows the distance range up to which the hypocentroid is calculated.

slightly greater than independent estimates from nearby receiver functions (31–34 km)[*Saunders et al.*, 1998; *Karabulut et al.*, 2013; *Tezel et al.*, 2013; *Vanacore et al.*, 2013; *Delph et al.*, 2015] and from regional waveform inversion studies (33 km) [*Horasan et al.*, 2002; *Fichtner et al.*, 2013]. Many of these studies support the presence of a midcrustal (10–18 km) low-velocity zone in western Turkey, but we do not see clear evidence for a reduction in velocity with depth in the form of a shadow zone (Figure S4).

4.1. 2011 Simav Aftershocks

We relocated a cluster of 195 events in the eastern Simav graben, including the 19 May 2011 main shock, 38 events preceding it (1969–2011), and 156 aftershocks (up to late 2013). This cluster benefited from excellent station coverage with 1536 arrival times for the location of the hypocentroid (distance <0.7°) and 26,002 readings for the cluster vectors (Figure S3a). We started by relocating the recent earthquakes using local station data, solving for depth once a robust velocity model was obtained (Table 2) and outliers were removed. Depths are highly dependent on the readings from near-source stations (<0.2°), so we first repicked *Pg* and *Sg* phases of 23 best-recorded earthquakes at the closest stations (SIMA and SMAA), using waveform data provided by the Kandilli Observatory. Then we introduced the older events into the cluster, fixing their depth at 15 km. Uncertainties for our calibrated epicenters are <1.5 km for modern events (2007–2013) and 1.9–3.4 km for older events (Figure 5 and Table S1). Though not formally defined, we estimate uncertainties in focal depth of between ∼2 km (for events with near-source recordings) to ∼4 km (for those without), through multiple inversions performed with perturbed velocity models and arrival times.

Our calibrated earthquake hypocenters are concentrated in a condensed (∼10 × 10 km) area near the eastern end of the Simav valley (Figure 5). Although they do not delineate a clear fault trend, the location of the main shock at the northern edge of the cluster provides some additional support toward our inference that the north dipping Simav fault was active during this sequence. The hypocentroid of the main shock lies ∼2 km SE of the center of the InSAR fault plane but is ∼10 km deeper. The depth range of the main shock and aftershock hypocenters is 10–22 km, indicating that they initiated directly below, rather than on, the principal slip plane of the main shock event as obtained from InSAR modeling. We further checked this result by performing four additional inversions using events with near-source recordings only, fixing the cluster depths at 5 km, 10 km, and 20 km. At fixed depths of 5–10 km, we find strong positive residuals between observed P_g and S_g arrivals and theoretical traveltimes over the near-source distance range 0–0.2°, consistent with these depths being
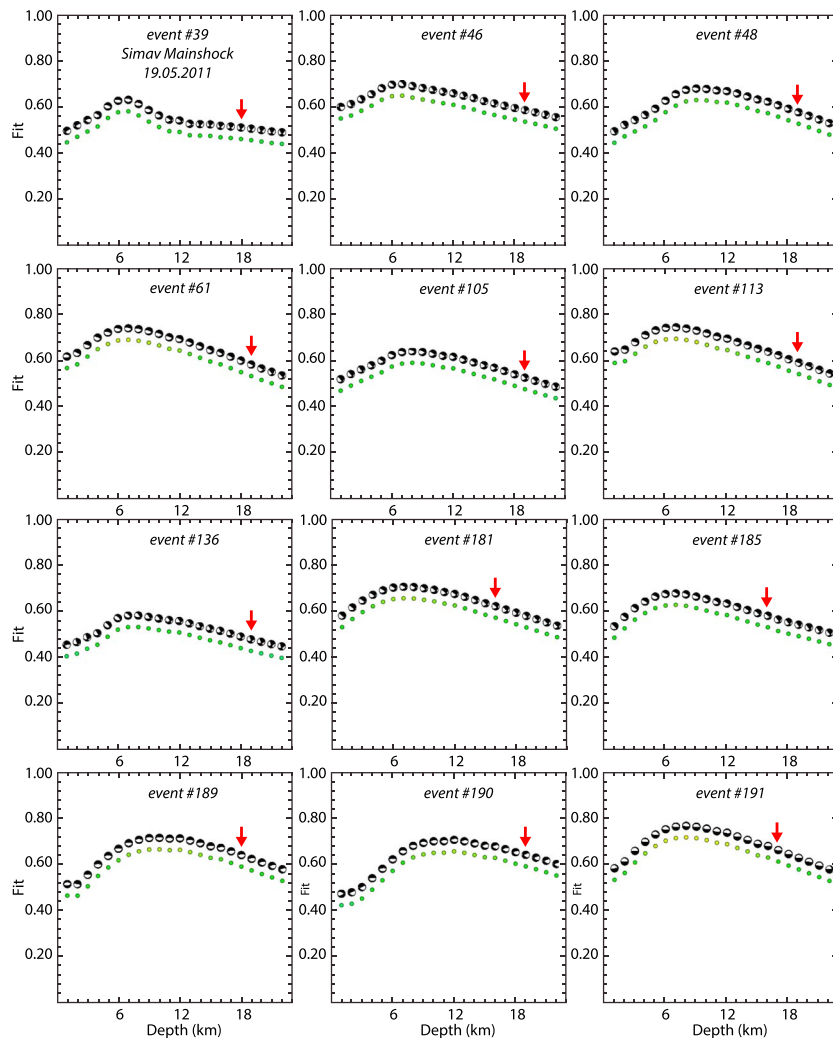
Figure 7. Goodness of fit and best fitting focal mechanism as a function of centroid depth from regional moment tensor analyses. Best fit solutions are listed in Table 4 and plotted in map view in Figure S5. At each 1 km increment in centroid depth, the best fitting mechanism is also plotted. Red arrows show the hypocenter depths calculated from calibrated relocations.

too shallow (Figure 6). There is no systematic residual when hypocentroid depths are manually determined (average ~15 km), while at 20 km, a strong negative residual appears.

By contrast, *Görgün* [2014] and *Demirci et al.* [2015] obtained aftershock depth ranges of 2–24 km and 2–16 km, respectively, using the double-difference relocation technique [*Waldhauser and Ellsworth*, 2000]. This algorithm is more sensitive to the velocity model, since the relative location problem is not separated from the absolute relocation problem and there is little emphasis on the uncertainties. The double-difference technique also does not include a concept similar to "cleaning," in which empirical reading errors are used to identify and flag outliers. We performed several inversions using *Görgün* [2014] epicenters, origin times, and chosen velocity model [from *Akyol et al.*, 2006]; all resulted in large residuals between observed and theoretical traveltimes at local and regional distances.

For eleven of the largest aftershocks (M_w 3.9–4.7), we complemented these focal (hypocenter) depths with estimates of centroid depth from regional waveform modeling, using the methods outlined in section 3.2. Preferred centroid depths are mostly 7–8 km, in close agreement with that of the main shock, but maxima in the fit as a function of centroid depth are less well defined for the smaller events probably due to their lower signal-to-noise ratio (Figure 7 and Table 4). Nevertheless, forcing the centroids deeper (approaching their hypocenter depths) introduces a strong strike-slip component that is conspicuously absent from previous

Table 4. Source Parameters for the Simav Main Shock and 11 Aftershocks From Regional Moment Tensor Inversion[a]

Event No.	Date	Time (UTC)	Depth (km)	Strike (°)	Dip (°)	Rake (°)	M_w
39	2011.05.19	20:15:22	7	285	55	280	5.8
46	2011.05.19	21:12:50	7	320	65	300	4.4
48	2011.05.19	21:33:10	9	290	60	290	4.1
61	2011.05.20	00:58:32	7	285	70	285	4.3
105	2011.05.27	07:43:36	8	295	65	300	4.4
113	2011.05.29	01:31:38	7	285	70	280	4.2
136	2011.06.27	21:28:50	8	325	65	305	3.9
181	2012.04.17	20:45:16	7	300	70	305	4.0
185	2012.04.26	22:05:32	7	300	70	295	4.7
189	2012.05.03	17:10:09	10	270	65	270	4.0
190	2012.05.03	21:45:16	12	105	35	290	4.2
191	2012.05.04	02:00:35	8	285	20	280	4.0

[a]See Table S1 for hypocenter parameters.

instrumental focal mechanisms within the region (Figure 2b). This implies that the discrepancy of 7–12 km between (shallower) aftershock centroid depths and (deeper) focal depths is real. We return to this point in section 5.1.

4.2. The 28 March 1970 Gediz Earthquake and Aftershocks

The 28 March 1970 Gediz earthquake (M_w 7.1) was one of the most destructive earthquakes in western Turkey's history, killing more than 1000 people and damaging or destroying ~ 20,000 buildings [*Taşdemiroğlu*, 1971; *Ambraseys and Tchalenko*, 1972]. It is the only instrumental earthquake within our study area known to have generated unequivocal, primary surface ruptures, in an unusual, "L"-shaped pattern that tracks across the foothills of the eastern Saphanedağ and northern Muratdağ ranges and the plains of the Gediz river basin [*Ambraseys and Tchalenko*, 1972] (Figure 2). The ruptures featured up to 2.7 m of normal slip on the ~15 km long ENE dipping Aşıkpaşa-Muhipler fault and up to 1.2 m of normal slip on the ~20 km long, north dipping Erdoğmuş-Hamamlar fault, with both faults also exhibiting minor left-lateral slip in places. Neither strand is coincident with larger breaks in the topography indicative of dominant Quaternary faulting, although trenching of the Erdoğmuş-Hamamlar fault by *Gürboğa-Deveci et al.* [2013] revealed evidence for two pale-oevents ~1000 years ago, hinting that the causative faults may be quite active during the Holocene. In addition, several shorter, NW-SE trending, uphill facing scarps and ridge-top fissures formed within hills in the hanging wall of the Aşıkpaşa-Muhipler fault. This region is composed of weak, calcareous marls and these features may represent sakungen formed by slumping rather than primary surface ruptures [*Ambraseys and Tchalenko*, 1972].

A first motions mechanism for the event by *McKenzie* [1978] is consistent with a NE dipping normal fault with a NW-SE strike, intermediate with respect to the trends of the two main surface ruptures, and with a rather shallow dip of 35° (Table 5). Teleseismic body waveform modeling by *Eyidoğan and Jackson* [1985] yielded a more complex source comprising five subevents. The first and second subevents strike NNW and W, respectively, accounting for the L-shaped surface fault trace, each with a dip of 35° and centroid depth of 10 km. The third and fourth subevents are required to match the shapes of the middle part of the modeled *P* and *SH* seismograms, and a fifth is needed to reproduce a large, long-period pulse observed at northern and northwestern azimuths. Intriguingly, the fifth subevent is deeper (15 km), shallower (20° dip), and of longer duration (14 s) than the earlier events and may therefore represent late slip on a north dipping, low-angle detachment.

However, subsequent waveform modeling by *Braunmiller and Nábělek* [1996] called into question the involvement of low-angle faulting. Noticing that the late pulse at north and NW azimuths also appeared in aftershock seismograms, they attributed it to structural (path) effects rather than source complications. Furthermore, they found that a single event with a mechanism similar to *McKenzie* [1978]'s first motion

Table 5. Source Parameters of Instrumentally Recorded Events in the Gediz Region[a]

Date	Time (UTC)	Latitude	Longitude	Depth (km)	Moment (Nm)	M_w	Strike1 (°)	Dip1 (°)	Rake1 (°)	Strike2 (°)	Dip2 (°)	Rake2 (°)	Reference	Data used
1970.03.28	21:02:23	39.21[h]	29.51[h]	18.0[h]	-	6.0m_b	-	-	-	-	-	-	ISC	Global traveltimes
	21:02:26	39.17[h]	29.54[h]	23.4[h]	-	6.0m_b	-	-	-	-	-	-	EHB	Global traveltimes
	21:02:25	39.17[h]	29.55[h]	24.4[h]	-	7.2	-	-	-	-	-	-	NEIC	Global traveltimes
	-	-	-	-	-	6.0	308	35	-90	128	55	-90	McK78	P wave first motions
	+4 s	-	-	10.0[c]	1.09 × 10^19	6.7	308	35	-90	128	55	-90	EJ85	Teleseismic long period P waveforms
	+8.5 s	-	-	10.0[c]	3.06 × 10^19	7.0	270	35	-110	114	57	-77	"	"
	-	-	-	10.0[c]	1.64 × 10^19	6.8	270	25	-90	90	65	-90	"	"
	+15 s	-	-	10.0[c]	7.7 × 10^18	6.6	329	48	-42	90	60	-130	"	"
	+24 s	-	-	15.0[c]	2.19 × 10^19	6.9	270	20	-90	90	70	-90	"	"
	-	-	-	**7.7[c]**	**5.05 × 10^19**	**7.1**	**304**	**41**	**-97**	**133**	**49**	**-84**	**BN96**	Teleseismic long-period body waves
1970.04.16	10:42:22	39.02[h]	29.91[h]	31.0[h]	-	5.4m_b	-	-	-	-	-	-	ISC	Global traveltimes
	10:42:25	38.99[h]	29.91[h]	36.1[h]	-	5.4	-	-	-	-	-	-	EHB	Global traveltimes
	10:42:18	39.00[h]	30.00[h]	9.0[h]	-	5.5	-	-	-	-	-	-	NEIC	Global traveltimes
	-	-	-	-	-	5.5	280	31	-100	112	60	-84	McK78	P wave first motions
	-	-	-	8.0[c]	2.7 × 10^17	5.6	280	31	-100	112	60	-84	EJ85	Teleseismic long-period P waveforms
	-	-	-	**7.8[c]**	**2.6 × 10^17**	**5.6**	**283**	**38**	**-78**	**88**	**53**	**-99**	**BN96**	Teleseismic long-period body waves
1970.04.19	13:29:36	39.03[h]	29.76[h]	18.0[h]	-	5.5m_b	-	-	-	-	-	-	ISC	Global traveltimes
	13:29:37	38.98[h]	29.77[h]	14.8[h]	-	5.5	-	-	-	-	-	-	EHB	Global traveltimes
	13:29:37	38.99[h]	29.77[h]	13.9[h]	-	5.6	-	-	-	-	-	-	NEIC	Global traveltimes
	-	-	-	-	-	5.4	284	66	-90	104	24	-90	McK78	P wave first motions
	+2.8 s	-	-	8.0[c]	2.9 × 10^17	5.7	284	66	-90	104	24	-90	EJ85	Teleseismic long-period P waveforms
	+7.6 s	-	-	8.0[c]	1.0 × 10^18	6.0	284	56	-90	104	34	-90	"	"
	-	-	-	8.0[c]	3.1 × 10^17	5.7	284	25	-90	104	65	-90	"	"
	+16 s	-	-	12.0[c]	3.4 × 10^17	5.7	284	25	-90	104	65	-90	"	"
	-	-	-	**9.6[c]**	**7.1 × 10^17**	**5.9**	**278**	**50**	**-93**	**102**	**40**	**-87**	**BN96**	Teleseismic long-period body waves
1971.05.25	05:43:26	39.052[h]	29.71[h]	15.7[h]	-	5.7m_b	-	-	-	-	-	-	ISC	Global traveltimes
	05:43:27	39.03[h]	29.73[h]	11.8[h]	-	5.7	-	-	-	-	-	-	EHB	Global traveltimes
	05:43:26	39.03[h]	29.73[h]	12.4[h]	-	5.5	-	-	-	-	-	-	NEIC	Global traveltimes
	-	-	-	-	-	5.8	298	55	-86	111	35	-96	McK78	P wave first motions
	-	-	-	6.0[c]	9.5 × 10^17	6.0	298	55	-77	96	37	-108	EJ85	Teleseismic long-period P waveforms
	-	-	-	**6.6[c]**	**6.5 × 10^17**	**5.9**	**297**	**51**	**-78**	**98**	**40**	**-104**	**BN96**	Teleseismic long-period body waves

[a]h and c are hypocenter and centroid parameters, respectively. References are: McK78-*McKenzie* [1978], EJ85-*Eyidoğan and Jackson* [1985], BN96-*Braunmiller and Nábělek* [1996]. Focal mechanisms displayed in Figure 2b are shown in bold.
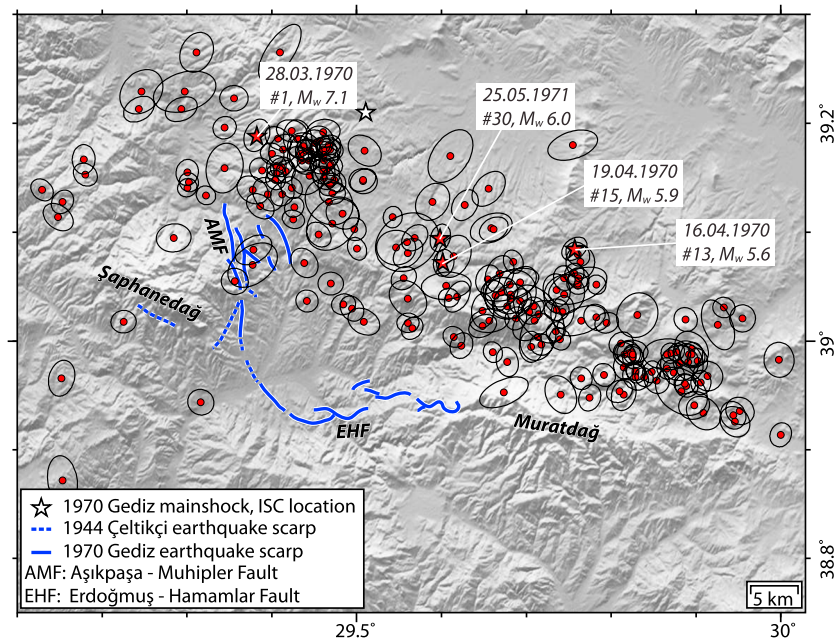
Figure 8. Epicenters of earthquakes in the Gediz cluster, with 90% confidence ellipses. Numbers and stars denote earthquakes with focal mechanisms in Tables 5 and S2. Surface ruptures of the 1944 Çeltikçi and 1970 Gediz earthquakes are taken from *Ambraseys and Tchalenko* [1972].

solution produced a better match to observed *SH* waveforms than more complex listric or multiple-event models.

Our Gediz cluster includes 198 earthquakes reported by the International Seismological Centre during the period 1970–2013. The ray paths used for direct calibration (Figure S3b) provide strong density and azimuthal coverage, providing 1133 short distance readings (distance <0.8°) used for hypocentroid location. The uncertainties in the locations, which are given by the length of the larger semiaxes of the confidence ellipses (L2 in Table S2), vary between ~1.0 and 3.5 km, with most events <2 km. The Gediz main shock and its largest aftershocks have uncertainties of 1–2 km (#1, #13, #15, and #30 in Table S2) which represents a significant improvement in accuracy over International Seismological Centre (ISC) locations. We initially fixed the focal depth to 15 km, and after the necessary cleaning, depths for the modern events that have phase readings at short epicentral distance are set by performing free depth inversions.

This cluster revealed a relatively narrow (~15 km wide), WNW-ESE trending band of seismicity. The calibrated location for the main shock is situated ~12 km southwest of its ISC location (Figure 8) and is now more consistent with the mapped L-shaped surface rupture [*Ambraseys and Tchalenko*, 1972] and with *Eyidoğan and Jackson* [1985]'s interpretation that the main shock nucleated on the NNW-SSE trending Aşıkpaşa-Muhipler fault, before rupturing unilaterally toward the southeast. There is no concentration of events at the intersection of the Aşıkpaşa-Muhipler and Erdoğmuş-Hamamlar faults, suggesting a relatively continuous linkage of these structures at depth. Single-event source models for this event indicate a rather shallow dip of ~35°, close to the lower bound of what is mechanically feasible in most normal faulting settings [*Jackson and White*, 1989]. However, there is no indication of aftershocks located along or around a deep, very shallow-angle (~20°), northward extension of this fault, as was suggested by *Eyidoğan and Jackson* [1985] on the basis of their multiple-event modeling.

There are concentrations of events associated with both terminations of the surface faulting, but seismicity also extends beyond the 1970 surface rupture, particularly toward the east where it may illuminate an eastern extension to the Erdoğmuş-Hamamlar fault along the northern margin of the Muratdağ range. There is a greater concentration of events beyond the southeastern rupture termination (i.e., in the direction of rupture propagation) than beyond the northwestern termination, in spite of the fact of that surface slip (and, thus, static stress change) is generally lower in the SE rupture zone than in the NW. This suggests that some of the southeastern aftershocks were triggered by transient surface waves, which were presumably largest at those

Table 6. Source Parameters of Instrumentally Recorded Events in the Demirci Region[a]

Date	Time (UTC)	Latitude	Longitude	Depth (km)	Moment (Nm)	M_w	Strike1 (°)	Dip1 (°)	Rake1 (°)	Strike2 (°)	Dip2 (°)	Rake2 (°)	Reference	Data used
1969.03.23	21:08:43	39.13^h	28.48^h	5.2^h	-	5.6	-	-	-	-	-	-	ISC	Global traveltimes
	21:08:45	39.12^h	28.49^h	15.2^h	-	5.6	-	-	-	-	-	-	EHB	Global traveltimes
	21:08:44	39.13^h	28.50^h	12.3^h	-	5.6	-	-	-	-	-	-	NEIC	Global traveltimes
	-	-	-	-	-	5.6	287	50	-64	70	47	-118	McK72	P wave first motions
	-	-	-	8.0^c	9.8×10^{17}	6.0	292	56	-90	112	34	-90	EJ85	Teleseismic long-period P waveforms
	-	-	-	**8.4^c**	**6.8×10^{17}**	**5.9**	**296**	**54**	**-88**	**112**	**36**	**-93**	**BN96**	Teleseismic long-period body waves
1969.03.25	13:21:12	39.06^h	28.41^h	9.6^h	-	4.9	-	-	-	-	-	-	ISC	Global traveltimes
	13:21:14	39.03^h	28.35^h	29.3^h	-	4.9	-	-	-	-	-	-	EHB	Global traveltimes
	13:21:36	39.20^h	28.47^h	48.9^h	-	5.5	-	-	-	-	-	-	NEIC	Global traveltimes
	-	-	-	-	-	5.6	288	51	-101	125	40	-77	McK72	P wave first motions
	-	-	-	8.0^c	1.7×10^{18}	5.5	288	51	-79	90	40	-104	EJ85	Teleseismic long-period P waveforms
	-	-	-	**9.9^c**	**8.8×10^{17}**	**6.0**	**307**	**44**	**-84**	**119**	**46**	**-96**	**BN96**	Teleseismic long-period body waves
1969.04.30	20:20:32	39.12^h	28.52^h	7.6^h	-	5.0	-	-	-	-	-	-	ISC	Global traveltimes
	20:34.60	39.14^h	28.55^h	14.5^h	-	5.0	-	-	-	-	-	-	EHB	Global traveltimes
	-	-	-	-	-	**5.1**	**288**	**55**	**-72**	**78**	**39**	**-114**	**McK72**	P wave first motions
1970.04.23	09:01:24	39.13^h	28.65^h	5.7^h	-	5.2	-	-	-	-	-	-	ISC	Global traveltimes
	09:01:29	39.12^h	28.67^h	35.0^h	-	5.2	-	-	-	-	-	-	EHB	Global traveltimes
	-	-	-	-	-	**5.2**	**266**	**40**	**-83**	**77**	**50**	**-96**	**McK78**	P wave first motions

[a] h and c are hypocenter and centroid parameters, respectively. References are McK72 — *McKenzie* [1972], McK78 — *McKenzie* [1978], EJ85 — *Eyidoğan and Jackson* [1985], and BN96 — *Braunmiller and Nábělek* [1996]. Focal mechanisms displayed in Figure 2b are shown in bold.
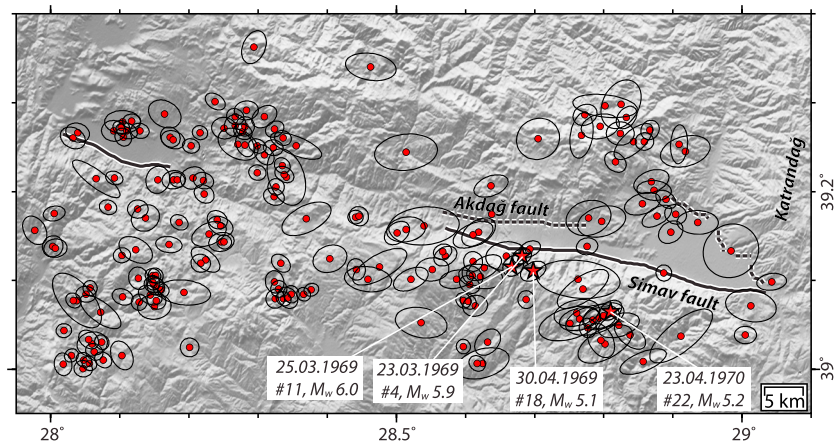
Figure 9. Epicenters of earthquakes in the Demirci cluster, with 90% confidence ellipses. Numbers and stars denote earthquakes with focal mechanisms in Tables 6 and S3.

azimuths, a phenomenon that has been noted for several other unilateral ruptures [*Gomberg et al.*, 2003]. The steeper northern slopes and gentler southern escarpment of Muratdağ may indicate long-term rotation of the footwall block, though the physiography is much less distinctive than for the Demircidağ range in the footwall of the Simav fault.

4.3. March 1969 Demirci Earthquakes and Aftershocks

The Demirci sequence started with M_w 5.9 and M_w 6.0 earthquakes on 23 and 25 March 1969, which damaged ~1700 buildings but did not cause any fatalities [*Ambraseys and Tchalenko*, 1972]. The heaviest damage occurred ~10 km north of the town of Demirci. There were unconfirmed reports of surface deformation in the hills of the western Simav graben [*Seyitoğlu*, 1997], although there are no robust indications of primary surface ruptures.

McKenzie [1972]'s first motion solution for the 23 March 1969 main shock supports an ~E-W striking normal mechanism with a component of oblique slip. Subsequent teleseismic body waveform modeling by *Eyidoğan and Jackson* [1985] and *Braunmiller and Nábeělek* [1996] indicate slip on a ~WNW-ESE trending normal fault with a centroid depth of 8.0 km (Table 6). None of these solutions could resolve the ambiguity in dip direction, since both nodal planes have plausible dips of 34°–56°. The second large event on 25 March 1969 has a similar first motion and initial teleseismic body waveform solution [*McKenzie*, 1972; *Eyidoğan and Jackson*, 1985], whereas *Braunmiller and Nábeělek* [1996]'s later analysis, which models *SH* as well as *P* seismograms, has a deeper centroid (10 km) and a NW-SE strike. Two subsequent aftershocks (30 April 1969 and 23 April 1970) were large enough for a first motions solution to be obtained, again indicating E-W oriented normal faulting [*McKenzie*, 1972, 1978].

Eyidoğan and Jackson [1985] suggested that the two largest events ruptured the south dipping Akdağ fault, on the northern margin of the Simav graben, because the trunk stream in the graben hugs the Akdağ fault rather than the north dipping Simav fault on the southern side. However, *Seyitoğlu* [1997] claimed that the earthquakes ruptured the north dipping Simav fault due to fresh fault surfaces they observed near the south side of the graben. The asymmetry of the graben may instead reflect the greater erodibility of metamorphic rocks in the footwall of the Simav fault compared to granitic rocks in the footwall of the Akdağ fault.

For the relocation of the Demirci sequence, we gathered a cluster of 190 events in the period 1969–2013. Good regional azimuthal coverage is available, and we utilized 1086 short distance arrival times (<0.85°, mostly *Pg* and *Sg*) (Figure S3c). A depth range of 9–22 km was obtained for the events with near-source readings, and for the remaining earthquakes a fixed depth of 14 km was used. Calibrated hypocenters have errors of 1–5 km with smaller uncertainties of <2 km for the largest events (Figure 9 and Table S3).

Our relocation places the hypocenters of the Demirci earthquakes of 23 and 25 March 1969 (M_w 5.9, M_w 6.0) in very close proximity to each other, a few kilometers south of the surface trace of the Simav fault. These events cannot therefore have ruptured the north dipping Simav fault, let alone a low-angle, northward extension of it as was proposed by *Seyitoğlu* [1997]. Instead, the relocated Demirci hypocenters, nodal plane dips (~35–55°),

and centroid depths (∼8–10 km) are consistent with slip on a deep portion of the south dipping Akdağ fault zone, which is marked at the surface by discontinuous escarpments on the north side of the Simav graben. However, the apparent lack of primary surface rupturing prevents us from ruling out slip on a north dipping fault, which would project to the surface somewhere along the gently dipping southern flank of Demircidağ (there are no obvious candidate surface faults in this area). Our analysis also reveals a SW-NE trending structure near the southwest corner of the cluster, in another area which lacks any mapped active faults.

5. Discussion

5.1. Mechanical Properties of the Seismogenic Layer

Well-recorded hypocenter depths in the eastern Simav basin are concentrated over a depth range of 10–22 km, which presumably marks the transition zone between brittle (velocity-weakening) and ductile (velocity-strengthening) behavior in the middle crust [*Scholz*, 2002]. However, there is a striking vertical separation between these focal depths and both the principal slip patch of the 2011 Simav main shock (∼6–10 km) and the aftershock centroid depths from regional waveform modeling (which range from 7 to 12 km). The main shock hypocenter—the point at which seismic slip initiated—lies directly below the resolvable slip patch rather than on it or at its lower boundary. The 13 M_w 3.9–4.7 aftershocks analyzed with regional waveforms (Table 4 and Figure 7) have centroid depths that are on average ∼9 km shallower than their focal depths, yet their source dimensions are probably no more than ∼2 km, implying that they too are initiating in areas of low slip, below rather than along the edge of their main rupture patches. Though surprising, these are not the first known examples of such behavior. The hypocenter of the 2000 Tottori, Japan earthquake (M_w 6.6) occurred at a depth of ∼14 km, at the lower edge of the main aftershock zone (6–12 km) and below the zone of resolvable slip (0–8 km), as if the earthquake crossed but left largely unruptured a large asperity [*Semmane et al.*, 2005]. The hypocenter of the 2014 South Napa, California earthquake (M_w 6.1) was located at a depth of ∼11 km, near the base of the principal aftershock zone (7–12 km) and below the main slip patch (0–8 km) [*Wei et al.*, 2015].

The Simav main shock rupture extended upward to a top depth of approximately 6 km, well short of the surface. However, surface faulting up dip of the rupture is clear in the topography, marked by the steep southern escarpment of the Simav graben. This begs the question how and when slip is accommodated on the shallow portion of the Simav fault. This shallow fault section may be velocity strengthening, particularly if composed of weak fault gouge, in which case it is likely to slide at slow rates as postseismic or interseismic creep [e.g., *Marone et al.*, 1991]. This inference is supported by the apparent absence of shallow aftershocks, as if dynamic stresses forced the main shock rupture into a velocity-strengthening layer [e.g., *Wei et al.*, 2015]. However, there are other plausible explanations for the upper termination of the 2011 rupture such as structural control by antithetic faulting [*Elliott et al.*, 2011] or by a discrete layer of weak rocks [*Nissen et al.*, 2011] and so we cannot rule out seismogenic slip in a future earthquake.

5.2. Regional Patterns of Normal Faulting

An interesting overall aspect of the last century of seismicity in the Simav-Gediz region is that by far the largest event—the 1970 Gediz earthquake (M_w 7.1)—occurred in an area of slower extension and indistinct surface faulting yet generated large surface breaks, while the well-defined and more rapidly extending Simav graben is associated with several smaller, M_w 5.0–6.0 events, none of which produced surface slip. This pattern highlights the difficulty in anticipating earthquake magnitude limits based on mapped fault segment lengths, even in areas of rather rapid continental deformation: without knowledge of the 1970 earthquake, the surface traces of the Aşıkpaşa-Muhipler and Erdoğmuş-Hamamlar faults would be difficult to discern even with modern satellite imagery. That said, our relocations also highlight the existence of a significant gap in larger instrumental events along the central section of the ∼40 km long, straight Simav fault, which poses a clear hazard to the area. We further demonstrate the value of calibrated hypocenters by using them to map an eastern continuation of the 1970 faulting in an area where active normal faulting is not currently universally recognized. A general observation is that though our study area lies at the northern edge of the Menderes Massif, a major metamorphic core complex, there is no support for involvement of seismogenic low-angle (<30° dipping) normal faulting in any of the recent large earthquake focal mechanisms or their aftershock distributions nor do we observe a consistent, significant component of right-lateral slip, contrary to published fault maps of the region [*Şaroğlu et al.*, 1992; *Emre et al.*, 2011].

6. Conclusions

Seismic waveform and InSAR modeling of the 2011 Simav earthquake reveal rupture of the steep, planar, north dipping Simav fault. The centroid depth was 7–9 km, but there was little or no slip in the upper few kilometers, indicating either that the shallow portion of the fault slips aseismically during a later stage in the earthquake cycle or that it may rupture in a future earthquake. More unusually, the hypocenters of the main shock and largest aftershocks were located at depths of 10–22 km and are systematically deeper than their own centroids, suggesting that they nucleated in a region of low coseismic slip. Similar focal depth ranges were obtained for modern events to the west and east. Seismicity in the central and western Simav graben is distributed off the main Simav fault, indicating activity on neighboring structures, and the hypocenters of the M_w 5.9, M_w 6.0 Demirci doublet are consistent with slip on the antithetic, south dipping Akdağ fault. Further east, seismicity includes some likely dynamically triggered aftershocks and reveals an eastern continuation of the 1970 Gediz earthquake faulting along the northern margin of the Muratdağ range. Larger earthquakes throughout the Simav-Gediz region involve moderately to steeply dipping planar faults with only small components of strike slip.

References

Aktuğ, B., et al. (2009), Deformation of western Turkey from a combination of permanent and campaign GPS data: Limits to block-like behavior, *J. Geophys. Res.*, *114*, B10404, doi:10.1029/2008JB006000.

Akyol, N., L. Zhu, B. J. Mitchell, H. Sözbilir, and K. Kekovalı (2006), Crustal structure and local seismicity in western Anatolia, *Geophys. J. Int.*, *166*(3), 1259–1269, doi:10.1111/j.1365-246X.2006.03053.x.

Ambraseys, N., and J. Jackson (1998), Faulting associated with historical and recent earthquakes in the Eastern Mediterranean region, *Geophys. J. Int.*, *133*(2), 390–406.

Ambraseys, N. N., and J. S. Tchalenko (1972), Seismotectonic aspects of the Gediz, Turkey, Earthquake of March 1970, *Geophys. J. R. Astron. Soc.*, *30*, 229–252, doi:10.1111/j.1365-246X.1972.tb05811.x.

Armijo, R., et al. (2005), Submarine fault scarps in the Sea of Marmara pull-apart (North Anatolian Fault): Implications for seismic hazard in Istanbul, *Geochem. Geophys. Geosyst.*, *6*, Q06009, doi:10.1029/2004GC000896.

Aziz Zanjani, A., A. Ghods, F. Sobouti, E. Bergman, G. Mortezanejad, K. Priestley, S. Madanipour, and M. Rezaeian (2013), Seismicity in the western coast of the South Caspian Basin and the Talesh Mountains, *Geophys. J. Int.*, *194*, 799–814, doi:10.1093/gji/ggt299.

Bergman, E. (2014), Multiple event relocation at the National Earthquake Information Center, *Tech. Rep.*, U.S. Geologicical Survey Award No. G11AP20016, Golden-Colorado.

Bergman, E. A., and S. C. Solomon (1990), Earthquake swarms on the Mid-Atlantic Ridge: Products of magmatism or extensional tectonics?, *J. Geophys. Res.*, *95*, 4943–4965, doi:10.1029/JB095iB04p04943.

Bozkurt, E., and H. Sözbilir (2004), Tectonic evolution of the Gediz Graben: Field evidence for an episodic, two-stage extension in western Turkey, *Geol. Mag.*, *141*, 63–79, doi:10.1017/S0016756803008379.

Braunmiller, J., and J. Nábělek (1996), Geometry of continental normal faults: Seismological constraints, *J. Geophys. Res.*, *101*, 3045–3052, doi:10.1029/95JB02882.

Croux, C., and P. J. Rousseeuw (1992), Time-efficient algorithms for two highly robust estimators of scale, in *Computational Statistics*, edited by C. Croux and P. J. Rousseeuw, pp. 411–428, Physica-Verlag, Berlin.

Delph, J. R., C. B. Biryol, S. L. Beck, G. Zandt, and K. M. Ward (2015), Shear wave velocity structure of the Anatolian Plate: Anomalously slow crust in southwestern Turkey,*Geophys. J. Int.*, *202*(1), 261–276, doi:10.1093/gji/ggv141.

Demirci, A., S. Özden, T. Bekler, D. Kalafat, and A. Pınar (2015), An active extensional deformation example: 19 May 2011 Simav earthquake ($M_w = 5.8$), Western Anatolia, Turkey, *J. Geophys. Eng.*, *12*(4), 552.

Dewey, J. F. (1988), Extensional collapse of orogens, *Tectonics*, *7*(6), 1123–1139, doi:10.1029/TC007i006p01123.

Elliott, J. R., B. Parsons, J. A. Jackson, X. Shan, R. A. Sloan, and R. T. Walker (2011), Depth segmentation of the seismogenic continental crust: The 2008 and 2009 Qaidam earthquakes, *Geophys. Res. Lett.*, *38*, L06305, doi:10.1029/2011GL046897.

Emre, Ö., T. Y. Duman, and S. Özalp (2011), 1:250000 scale Active Fault Map Series of Turkey, Kutahya (NJ 35-4) Quadrangle, *Serial Number 10*, General Directorate of Mineral Research and Exploration, Ankara, Turkey.

Eyidoğan, H., and J. Jackson (1985), A seismological study of normal faulting in the Demirci, Alaşehir and Gediz earthquakes of 1969–70 in western Turkey: Implications for the nature and geometry of deformation in the continental crust, *J. Geophys. Res.*, *81*, 569–607, doi:10.1111/j.1365-246X.1985.tb06423.x.

Fichtner, A., J. Trampert, P. Cupillard, E. Saygin, T. Taymaz, Y. Capdeville, and A. Villaseñor (2013), Multiscale full waveform inversion, *Geophys. J. Int.*, *194*(1), 534–556, doi:10.1093/gji/ggt118.

Fredrich, J., R. McCaffrey, and D. Denham (1988), Source parameters of seven large Australian earthquakes determined by body waveform inversion, *Geophys. J. Int.*, *95*, 1–13, doi:10.1111/j.1365-246X.1988.tb00446.x.

Futterman, W. I. (1962), Dispersive body waves, *J. Geophys. Res.*, *67*, 5279–5291, doi:10.1029/JZ067i013p05279.

Ghods, A., M. Rezapour, E. Bergman, G. Mortezanejad, and M. Talebian (2012), Relocation of the 2006 M_w 6.1 Silakhour, Iran, earthquake sequence: Details of fault segmentation on the main recent fault, *Bull. Seismol. Soc. Am.*, *102*(1), 398–416, doi:10.1785/0120110009.

Gomberg, J., P. Bodin, and P. A. Reasenberg (2003), Observing earthquakes triggered in the near field by dynamic deformations, *Bull. Seismol. Soc. Am.*, *93*, 118–138, doi:10.1785/0120020075.

Görgün, E. (2014), Source characteristics and Coulomb stress change of the 19 May 2011 M_w 6.0 Simav-Kütahya earthquake, Turkey, *J. Asian Earth. Sci.*, *87*, 79–88, doi:10.1016/j.jseaes.2014.02.016.

Gürboğa, Ş. (2013), 28 March 1970 Gediz earthquake fault, western Turkey: Palaeoseismology and tectonic significance, *Int. Geol. Rev.*, *55*(10), 1191–1201, doi:10.1080/00206814.2013.771420.

Gürboğa-Deveci, Ş., A. Koçyiğit, and G. Ruffet (2013), Episodic two-stage extensional evolutionary model for southwestern Anatolian graben-horst system: New field data from the Erdoğmuş-Yenigediz graben (Kütahya), *J. Geodyn.*, *65*, 176–198, doi:10.1016/j.jog.2012.06.007.

Herrmann, R. B., H. Benz, and C. J. Ammon (2011), Monitoring the earthquake source process in North America, *Bull. Seismol. Soc. Am.*, *101*, 2609–2625, doi:10.1785/0120110095.

Hetzel, R., U. Ring, C. Akal, and M. Troesch (1995), Miocene NNE-directed extensional unroofing in the Menderes Massif, southwestern Turkey, *J. Geol.*, *152*(4), 639–654, doi:10.1144/gsjgs.152.4.0639.

Hetzel, R., H. Zwingmann, A. Mulch, K. Gessner, C. Akal, A. Hampel, T. Güngör, R. Petschick, T. Mikes, and F. Wedin (2013), Spatiotemporal evolution of brittle normal faulting and fluid infiltration in detachment fault systems: A case study from the Menderes Massif, western Turkey, *Tectonics*, *32*(3), 364–376, doi:10.1002/tect.20031.

Horasan, G., L. Gülen, A. Pınar, D. Kalafat, N. Özel, H. S. Kuleli, and A. M. Işıkara (2002), Lithospheric structure of the Marmara and Aegean Regions, Western Turkey, *Bull. Seismol. Soc. Am.*, *92*(1), 322–329, doi:10.1785/0120000813.

Işık, V., and O. Tekeli (2001), Late orogenic crustal extension in the northern Menderes massif (western Turkey): Evidence for metamorphic core complex formation, *Int. J. Earth Sci.*, *89*(4), 757–765, doi:10.1007/s005310000105.

Jackson, J. A., and N. J. White (1989), Normal faulting in the upper continental crust: Observations from regions of active extension, *J. Struct. Geol.*, *11*(1), 15–36.

Jordan, T. H., and K. A. Sverdrup (1981), Teleseismic location techniques and their application to earthquake clusters in the South-Central Pacific, *Bull. Seismol. Soc. Am.*, *71*, 1105–1130.

Karabulut, H., A. Paul, T. Afacan Ergün, D. Hatzfeld, D. M. Childs, and M. Aktar (2013), Long-wavelength undulations of the seismic Moho beneath the strongly stretched Western Anatolia, *Geophys. J. Int.*, *194*, 450–464, doi:10.1093/gji/ggt100.

Kennett, B. L. N., E. R. Engdahl, and R. Buland (1995), Constraints on seismic velocities in the Earth from traveltimes, *Geophys. J. Int.*, *122*, 108–124, doi:10.1111/j.1365-246X.1995.tb03540.x.

Kind, R., T. Eken, F. Tilmann, F. Sodoudi, T. Taymaz, F. Bulut, X. Yuan, B. Can, and F. Schneider (2015), Thickness of the lithosphere beneath Turkey and surroundings from S-receiver functions, *Solid Earth*, *6*(3), 971–984, doi:10.5194/se-6-971-2015.

Koçyiğit, A., A. Yusufoğlu, and E. Bozkurt (1999), Evidence from the Gediz graben for episodic two-stage extension in western Turkey, *J. Geol. Soc.*, *156*, 605–616, doi:10.1144/gsjgs.156.3.0605.

Langston, C. A., and D. V. Helmberger (1975), A procedure for modelling shallow dislocation sources, *Geophys. J. R. Astron. Soc.*, *42*(1), 117–130.

Le Pichon, X., and J. Angelier (1979), The Hellenic arc and trench system: A key to the neotectonic evolution of the eastern Mediterranean area, *Tectonophysics*, *60*, 1–42, doi:10.1016/0040-1951(79)90131-8.

Lohman, R. B., M. Simons, and B. Savage (2002), Location and mechanism of the Little Skull Mountain earthquake as constrained by satellite radar interferometry and seismic waveform modeling, *J. Geophys. Res.*, *107*(B6), 2118, doi:10.1029/2001JB000627.

Maggi, A., J. A. Jackson, K. Priestley, and C. Baker (2000), A re-assessment of focal depth distributions in southern Iran, the Tien Shan and northern India: Do earthquakes really occur in the continental mantle?, *Geophys. J. Int.*, *143*, 629–661, doi:10.1046/j.1365-246X.2000.00254.x.

Marone, C. J., C. H. Scholz, and R. Bilham (1991), On the mechanics of earthquake afterslip, *J. Geophys. Res.*, *96*(B5), 8441–8452.

McCaffrey, R., and G. Abers (1988), SYN3: A program for inversion of teleseismic body wave forms on microcomputers, *Air Force Geophysical Laboratory Tech. Rep.*, Hanscomb Air Force Base, Massachusetts.

McCaffrey, R., P. Zwick, and G. Abers (1991), SYN4 Program, *Tech. Rep.*, IASPEI Software Library. [Available at https://scholar.google.com/scholar_lookup?title=SYN4%20Program&author=R.%20McCaffrey&author=P.%20Zwick&author=G.%20Abers&publication_year=1991&journal=IASPEI%20Software%20Library&volume=3&pages=81-166.]

McKenzie, D. (1972), Active tectonics of the Mediterranean region, *Geophys. J. Int.*, *30*, 109–185, doi:10.1111/j.1365-246X.1972.tb02351.x.

McKenzie, D. (1978), Active tectonics of the Alpine-Himalayan belt: The Aegean Sea and surrounding regions, *Geophys. J. R. Astron. Soc.*, *55*(1), 217–254, doi:10.1111/j.1365-246X.1978.tb04759.x.

Molnar, P., and H. Lyon-Caen (1989), Fault plane solutions of earthquakes and active tectonics of the Tibetan Plateau and its margins, *Geophys. J. Int.*, *99*, 123–154.

Nissen, E., M. Tatar, J. A. Jackson, and M. B. Allen (2011), New views on earthquake faulting in the Zagros fold-and-thrust belt of Iran, *Geophys. J. Int.*, *186*, 928–944.

Nyst, M., and W. Thatcher (2004), New constraints on the active tectonic deformation of the Aegean, *J. Geophys. Res.*, *109*, B11406, doi:10.1029/2003JB002830.

Okada, Y. (1985), Surface deformation due to shear and tensile faults in a half-space, *Bull. Seismol. Soc. Am.*, *75*, 1135–1154.

Purvis, M., and A. Robertson (2004), A pulsed extension model for the Neogene Recent E W-trending Alaşehir Graben and the NE SW-trending Selendi and Gördes Basins, western Turkey, *Tectonophysics*, *391*, 171–201, doi:10.1016/j.tecto.2004.07.011.

Reilinger, R., et al. (2006), GPS constraints on continental deformation in the Africa-Arabia-Eurasia continental collision zone and implications for the dynamics of plate interactions, *J. Geophys. Res.*, *111*, B05411, doi:10.1029/2005JB004051.

Rosen, P. A., S. Henley, G. Peltzer, and M. Simons (2004), Update repeat orbit interferometry package released, *Eos Trans. AGU*, *85*, 47–47, doi:10.1029/2004EO050004.

Şaroğlu, F., Ö. Emre, and İ. Kuşçu (1992), *Active Fault Map of Turkey*, General Directorate of Mineral Research and Exploration, Ankara, Turk.

Saunders, P., K. Priestley, and T. Taymaz (1998), Variations in the crustal structure beneath western Turkey, *Geophys. J. Int.*, *134*(2), 373–389, doi:10.1046/j.1365-246x.1998.00571.x.

Scholz, C. H. (2002), *The Mechanics of Earthquakes and Faulting*, Cambridge Univ. Press, New York.

Semmane, F., F. Cotton, and M. Campillo (2005), The 2000 Tottori earthquake: A shallow earthquake with no surface rupture and slip properties controlled by depth, *J. Geophys. Res.*, *110*, 03306, doi:10.1029/2004JB003194.

Sengör, A. M. C. (1987), Cross-faults and differential stretching of hanging walls in regions of low-angle normal faulting: Examples from western Turkey, *Geol. Soc. London Spec. Publ.*, *28*, 575–589, doi:10.1144/GSL.SP.1987.028.01.38.

Sengör, A. M. C., and Y. Yılmaz (1981), Tethyan evolution of Turkey: A plate tectonic approach, *Tectonophysics*, *75*, 181–241, doi:10.1016/0040-1951.

Seyitoğlu, G. (1997), Late Cenozoic tectono-sedimentary development of Selendi and Usak-Güre basins: A contribution to the discussion on the development of east-west and north-trending basins in western Turkey, *Geol. Mag.*, *134*, 163–175.

Seyitoğlu, G., and B. Scott (1991), Late Cenozoic crustal extension and basin formation in West Turkey, *Geol. Mag.*, *128*(2), 155–166, doi:10.1017/S0016756800018343.

Taşdemiroğlu, M. (1971), The 1970 Gediz earthquake in Western Anatolia, Turkey, *Bull. Seismol. Soc. Am.*, *61*, 1507–1527.

Taymaz, T., and S. Price (1992), The 1971 May 12 Burdur earthquake sequence, SW Turkey: A synthesis of seismological and geological observations, *Geophys. J. Int.*, *108*, 589–603, doi:10.1111/j.1365-246X.1992.tb04638.x.

Taymaz, T., J. Jackson, and D. McKenzie (1991), Active tectonics of the north and central Aegean Sea, *Geophys. J. Int.*, *106*(2), 433–490, doi:10.1111/j.1365-246X.1991.tb03906.x.

Tezel, T., T. Shibutani, and B. Kaypak (2013), Crustal thickness of Turkey determined by receiver function, *J. Asian Earth. Sci.*, *75*, 36–45, doi:10.1016/j.jseaes.2013.06.016.

Thomson, S. N., and U. Ring (2006), Thermochronologic evaluation of postcollision extension in the Anatolide orogen, western Turkey, *Tectonics*, *25*, TC3005, doi:10.1029/2005TC001833.

Tiryakioğlu, İ., M. Floyd, S. Erdoğan, E. Gülal, S. Ergintav, S. McClusky, and R. Reilinger (2013), GPS constraints on active deformation in the Isparta Angle region of SW Turkey, *Geophys. J. Int.*, *195*, 1455–1463, doi:10.1093/gji/ggt323.

van Hinsbergen, D. (2010), A key extensional metamorphic complex reviewed and restored: The Menderes Massif of western Turkey, *Earth Sci. Rev.*, *102*, 60–76, doi:10.1016/j.earscirev.2010.05.005.

van Hinsbergen, D. J. J., M. J. Dekkers, E. Bozkurt, and M. Koopman (2010), Exhumation with a twist: Paleomagnetic constraints on the evolution of the Menderes metamorphic core complex, western Turkey, *Tectonics*, *29*, TC3009, doi:10.1029/2009TC002596.

Vanacore, E., T. Taymaz, and E. E. Saygın (2013), Moho structure of the Anatolian Plate from receiver function analysis, *Geophys. J. Int.*, *193*(1), 329–337, doi:10.1093/gji/ggs107.

Waldhauser, F., and W. Ellsworth (2000), A double-difference earthquake location algorithm: Method and application to the northern Hayward fault, CA, *Bull. Seismol. Soc. Am.*, *90*(6), 1353–1368, doi:10.1785/0120000006.

Walker, R., E. Bergman, W. Szeliga, and E. Fielding (2011), Insights into the 1968–1997 Dasht-e-Bayaz and Zirkuh earthquake sequences, eastern Iran, from calibrated relocations, InSAR and high-resolution satellite imagery, *Geophys. J. Int.*, *187*, 1577–1603, doi:10.1111/j.1365-246X.2011.05213.x.

Wei, S., S. Barbot, R. Graves, J. J. Lienkaemper, T. Wang, K. Hudnut, Y. Fu, and D. Helmberger (2015), The 2014 M_w 6.1 South Napa earthquake: A unilateral rupture with shallow asperity and rapid afterslip, *Seismol. Res. Lett.*, *86*(2A), 344–354.

Westaway, R. (1990), Block rotation in western Turkey: 1. Observational evidence, *J. Geophys. Res.*, *95*(B12), 19,857–19,884, doi:10.1029/JB095iB12p19857.

Wright, T. J., B. E. Parsons, J. A. Jackson, M. Haynes, E. J. Fielding, P. C. England, and P. J. Clarke (1999), Source parameters of the 1 October 1995 Dinar (Turkey) earthquake from SAR interferometry and seismic bodywave modelling, *Earth Planet. Sci. Lett.*, *172*, 23–37.

Yılmaz, Y., S. C. Genc, F. Gurer, M. Bozcu, K. Yilmaz, Z. Karacik, S. Altunkaynak, and A. Elmas (2000), When did the western Anatolian grabens begin to develop?, *Geol. Soc. London Spec. Publ.*, *173*, 353–384, doi:10.1144/GSL.SP.2000.173.01.17.

Yolsal-Çevikbilen, S., T. Taymaz, and C. Helvacı (2014), Earthquake mechanisms in the Gulfs of Gökova, Sığacık, Kuşadası, and the Simav Region (western Turkey): Neotectonics, seismotectonics and geodynamic implications, *Tectonophysics*, *635*, 100–124, doi:10.1016/j.tecto.2014.05.001.

Zülfikar, C., Y. Kamer, and E. Vuran (2011), May 19, 2011 Kütahya-Simav Earthquake, Tech. Rep., Boğaziçi University, Kandilli Observatory and Earthquake Research Institute, Bebek, Istanbul.

Zwick, P., R. McCaffrey, and G. Abers (1994), *MT5 Program*, IASPEI Software Library 4. [Available at https://scholar.google.com/scholar_lookup?title=MT5%20Program&author=P.%20Zwick&author=R.%20McCaffrey&author=G.%20Abers&publication_year=1994&journal=IASPEI%20Software%20Library&volume=4.]